ORNL/TM-2021/2341
NFE-19-07798

Computational Fluid Dynamics Simulations to Support Efficiency Improvements in Aluminum Smelting Process

Nithin S. Panicker
Rajneesh Chaudhary
Marc-Olivier G. Delchini
Vivek M. Rao
Prashant K. Jain

Approved for Public Release.

December 2021

OAK RIDGE National Laboratory

ORNL IS MANAGED BY UT-BATTELLE LLC FOR THE US DEPARTMENT OF ENERGY

ORNL/TM-2021/2341
NFE-19-07798

Nuclear Energy and Fuel Cycle Division

COMPUTATIONAL FLUID DYNAMICS SIMULATIONS TO SUPPORT EFFICIENCY IMPROVEMENTS IN ALUMINUM SMELTING PROCESS

Nithin S. Panicker*
Rajneesh Chaudhary†
Marc-Olivier G. Delchini*
Vivek M. Rao*
Prashant K. Jain*

* Oak Ridge National Laboratory
†Alcoa Technical Center, Alcoa USA Corporation

December 2021

Prepared by
OAK RIDGE NATIONAL LABORATORY
Oak Ridge, TN 37831-6283
managed by
UT-BATTELLE LLC
for the
US DEPARTMENT OF ENERGY
under contract DE-AC05-00OR22725

CONTENTS

LIST OF FIGURES

LIST OF TABLES

ABBREVIATIONS

ACD	anode-to-cathode distance
AMO	Advanced Manufacturing Office
BC	boundary condition
CAD	computer-aided design
CE	current efficiency
CFD	computational fluid dynamics
cryolite	dissolution of solids in a molten electrolyte
DOE	US Department of Energy
DPM	discrete particle model
EERE	Office of Energy Efficiency and Renewable Energy
HD	heat of dissolution
HPC	high-performance computing
HPC4EI	High-Performance Computing for Energy Innovation
IC	initial condition
LES	large-eddy simulation
MHD	magnetohydrodynamics
NREL	National Renewable Energy Laboratory
ORNL	Oak Ridge National Laboratory
PIV	particle image velocimetry
RANS	Reynolds-averaged Navier Stokes
Ridge	Oak Ridge National Laboratory
RS	Reynolds stress
TKE	turbulent kinetic energy
VOF	volume of fluid

NOMENCLATURE

p	pressure ($\mathrm{N/m^2}$)
u	velocity ($\mathrm{m/s}$)
T	temperature (K)
Y	mass fraction (-)
k	turbulent kinetic energy ($\mathrm{m^2/s^2}$)
α	volume fraction (-)
ρ	density ($\mathrm{kg/m^3}$)
μ	dynamic viscosity (Pa - s)
Cp	heat capacity ($\mathrm{J/Kg\ K}$)
k	thermal conductivity ($\mathrm{W/m\ K}$)
d	particle size (m)
D	diffusion coefficient ($\mathrm{m^2/s}$)
J	current density ($\mathrm{A/m^2}$)
B	magnetic field (T)
L	lorentz force ($\mathrm{N/m^3}$)
σ	conductivity ($\mathrm{S/m}$)
g	gravity ($\mathrm{m/s^2}$)

ABSTRACT

Smelting is broadly described as the extraction of a metal from its ore. In the United States, aluminum is commonly produced by smelting alumina in bauxite using the Hall-Héroult process. Optimization of equipment and processes in conventional smelting is crucial to enhancing process efficiency and productivity, is necessary for improving the techno-economic feasibility, which directly manifests as the growth of the American economy. To achieve optima, insightful data on the multiphysics phenomena that are inherent to the process must be obtained through physical investigation or high-fidelity numerical simulations. The resolution of relevant scales in time and space for smelting operations requires intensive, high-performance computing (HPC) simulations. Hostile operating conditions limit physical data acquisition to specific techniques; therefore, these data do not describe the multiscale interaction of simultaneous effects. Fortunately, in recent decades, significant advancements in computing hardware and computational methods have made the numerical resolution of such a complex process possible. In this study, a high-fidelity simulation of aluminum smelting was performed using an open-source tool, OpenFOAM, which analyzed many parameters characteristic to underlying phenomena. A multiphysics model based on the Eulerian-Eulerian multifluid approach was adopted. This model can resolve critical issues in the electrolytic smelting of aluminum, such as bubbling of carbon dioxide from the anode(s), magnetohydrodynamics from electromagnetic effects, ionic dissolution of the alumina in the electrolyte, and the evolution of thermal profiles. This study provides valuable connectivity for characteristic data that can direct the future designs of efficient smelters.

A basic framework to model and simulate the smelting process using OpenFOAM is presented for user modification in keeping with process development. Of relevance to the flow field, a detailed investigation of vortices produced by bubble motion and electromagnetics is discussed, along with their impact on the evolution of thermal profiles. The predictions show small-scale vortices in the clearance between the anode and cathode caused by magnetic forces. Predictions also indicate relatively large-scale vortices in the inter-anode space resulting from carbon dioxide rising through the electrolytic flow field. The formation of vortices at the edges of anodes was shown to direct alumina charged by the feeder to the bottom of the anodes, thus preventing the entrapment of gas bubbles in the periphery of the bottom of the anode. Symmetry was observed in the location of cold spots in the electrolytic mixture in the vicinity of the feeder. Cold spots were also observed in the clearance between the anode and cathode due to the flow's transmission of unconverted alumina to this region.

1. STATEMENT OF OBJECTIVES

1.1 A BACKGROUND ON SMELTING OF ALUMINA TO PRODUCE ALUMINUM

Aluminum production is crucial for the US economy and other countries that depend on aluminum for various applications. Aluminum is typically produced using the Hall-Héroult process. A simple Hall–Héroult process electrolytic cell (see Figure 1) consists of an anode and cathode dipped into a molten bath of cryolite (Na_3AlF_6) maintained at a temperature of 960-970℃.

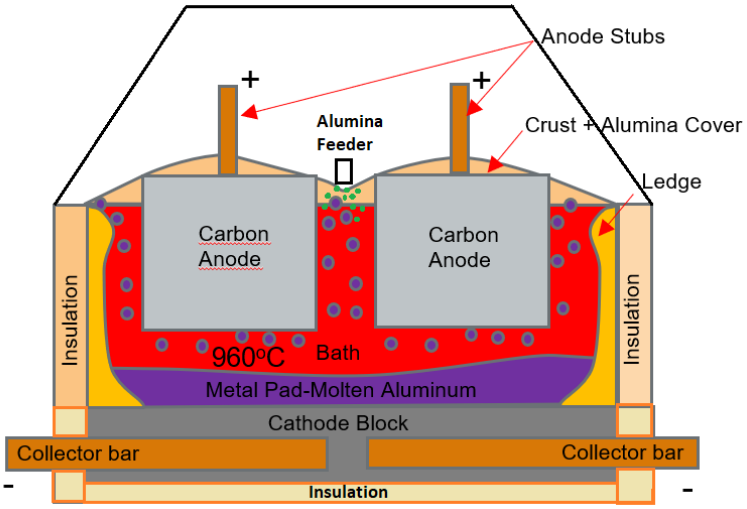

Figure 1. Aluminum smelting cell.

During production, direct current is passed continuously from anode to cathode. Powdered alumina (Al_2O_3) is fed through the hopper and dissolves into the electrolytic bath, a mixture of sodium fluoride (NaF) and aluminum fluoride (AlF_3), to form aluminum oxyfluoride ($Al_2OF_2^{6-}$). The oxyfluorides react with the anode material (graphite) to produce carbon dioxide (CO_2) and AlF_3. As the reaction in the anode progresses, the AlF_3 present in the bath is chemically reduced by the cathode to produce aluminum, which then melts into a pool above the metal pad (see Figure 1). Aluminum manufacturing is an energy-intensive process that is also responsible for the significant emission of greenhouse gases. Therefore, it is imperative to formulate strategies to reduce energy consumption and greenhouse emissions.

Optimization of the manufacturing process could be achieved by gaining detailed knowledge of the complex flow physics inside the electrolytic cell. The flow inside an electrolytic cell during operation is complex, involving multiphase interactions (gas, liquid, and solid) resulting in multiple physics: constant agitation of the bath from the rising CO_2 bubbles, alumina dissolution and diffusion across the cell, and magnetohydrodynamics (MHD) effect in anode-cathode spacing, and on the metal pad. Detailed measurements of velocity, current, mass transport, and other factors are required to better understand the flow inside an electrolytic cell. Because of the high operating temperature and hostile chemical environment, it is not always possible to directly measure such quantities from an operating electrolytic cell. It is also not possible to gauge the cell's behavior under extreme operating conditions. Computational fluid dynamics (CFD)–based modeling and simulation of the smelting process is an ideal alternative for extracting flow physics and studying the impacts of different electrolytic cell designs on energy consumption and CO_2 emissions. CFD-based studies of complex physical processes are gaining more attention due to the advancement of computational resources and more advanced mathematical models that can capture the complex physics involved in processes like smelting. CFD-based modeling

and simulation of the aluminum smelting process gained popularity only in the last decade. A review of the CFD modeling and simulation work performed in the literature for the smelting process is presented below.

1.2 COMPUTATIONAL SIMULATION OF ALUMINUM PRODUCTION: A REVIEW

1.2.1 Multifluid Model Studies

Le it al. (Li, et al., 2011) used a multifluid flow model with three phases—metal, bath, and gas bubbles—along with electromagnetics to investigate the metal-bath deformation and current distribution. A current efficiency (CE) model was coupled to the CFD model based on the mass transfer of aluminum from the bath to the metal phase. A 300-kA cell was used to conduct the studies. Predictions of metal-bath deformations using the three-phase and two-phase models (bath, metal) were nearly the same, indicating that a two-phase model is sufficient to predict the metal-bath deformation. A negative correlation between the CE and the metal-bath interface deformation can be observed in the study results. Li et al. concluded that the CFD model presented in their work could be used to optimize CE for smelting cells.

Feng et al. (Feng, et al., 2011) used the multifluid flow model with two phases—bath and gas bubbles—to study the alumina distribution inside the smelting cell. The model used in their study neglects the dissolution of alumina solids and the effect of electromagnetics flow in dispersing the dissolved alumina. Feng et al. concluded that there could be ~ 1wt% spatial variation in the alumina concentration across the cell, and the diffusion of alumina across the anode-to-cathode (ACD) space is much smaller than that across the central channels.

Zhang et al. (Zhang, et al., 2014) used a multifluid model like that used by Feng et al. (Feng, et al., 2011); however, the model used by Zhang et al. was also coupled to electromagnetics to gain an understanding of how bubble-driven flow and electromagnetics affect alumina mixing. They carried out their numerical investigation on a 300 kA cell with 20×2 anodes. They concluded that the bubble-driven flow dispersed alumina in the local areas more quickly than in the global region; however, the flow from electromagnetics played a crucial role in long-range mixing, indicating that it is essential to consider both the dispersion mechanisms in a CFD model to study alumina mixing.

Wang et al. (Wang, et al., 2014) used a multifluid model with three phases—bath, gas bubbles, and metal—coupled with the electromagnetics model, to compare the performance of a smelting cell with a dimpled cathode and a flat cathode. With the dimpled cathode, film formation on the gas bubble underneath the anode for the cell was lower than that of the flat cathode. The lower film formation allowed the dimpled cathode cell to provide superior (CE) over the flat cathode cell. The solid structures on the dimpled cathode cell dissipated the vortices that induce bath-metal interface fluctuation. Therefore, Wang et al. concluded that the dimpled cathode cell could be used with less ACD space than that used in traditional flat cathode cells, significantly increasing the energy efficiency.

Zhan et al. (Zhan, et al., 2014) performed a detailed study of the alumina dissolution process in a traditional smelting cell using the multifluid model coupled to a population balance model. They considered two bins for the particles—small and large. The small particle sizes ranged from 20 to 200 μm, and the large particle sizes ranged from 2 to 10 mm. It was assumed that (1) the dissolution of small particles was controlled by mass transfer, and (2) the bath temperature controlled the large particles. Therefore, separate dissolution models were developed for small and large particles, and these were then coupled to the CFD model. Zhan et al. observed that the small particles quickly dissolve and disappear in the vicinity of the feeders because of large specific areas. As a result of the low specific area, the large particles dissolve gradually as they settle toward the bottom of the cell. Zhan et al. also conducted studies to analyze the impacts of the bath diffusion coefficient and superheat on dissolution.

Einarsrud et al. (Einarsrud, et al., 2017) developed a simulation model based on a multifluid model to study the smelting process in an industrial smelting cell. The bubble production and dynamics were modeled using a volume of fluid (VOF) approach. They considered two phases—bath and bubble—along with electromagnetics. They introduced bath electrical conductivity as a function of gas fraction into their CFD model, which predicts current fluctuations in the cell caused by gas buildup. The dissolution rate of alumina was modeled based on empirical data for an industrial bath without considering the effects of mass or heat transfer. They studied the evolution of different electrochemical species inside the bath from electrochemical reactions and bubble- and electromagnetics-driven flow. They concluded that the qualitative trend observed was reasonable compared to industrial test results. They also concluded that their modeling framework could help improve the feeding strategies for reducing anode effects and could also help determine the impact of current fluctuations on the consumption of alumina in specific areas of the anode.

Cubeddu et al. (Cubeddu, et al., 2019) developed a three-phase multifluid model representing bath, bubbles, and metal dynamics to study bubble-driven flow's impact on bath-metal interface fluctuation. They performed a 2D CFD study on a geometry corresponding to a transverse cross-section of a typical smelting cell. The CO_2 production under the anode and the aluminum production at the bath-metal interface were modeled based on the current passing through the cell. They observed that the motion of gas under the anode and the release to the atmosphere caused swirls on the bath over the metal phase, leading to significant local fluctuations on the bath-metal interface. Moreover, they concluded that their multifluid-based model could predict the periodic nature of the CO_2 gas bubble buildup and release under the anode.

1.2.2 Interface-Tracking approach: Volume of Fluid (VOF)

Hua et al. (Hua, et al., 2018) used the VOF model with two phases—bath and metal—to investigate the bath-metal interface deformation on a 15 × 2 smelting cell under various conditions: with and without a flat metal-bath interface, with and without flow-induced current, with and without flow-induced magnetic field, and with different central channel gaps. They concluded that the accurate prediction of bath-metal interface deformation requires that bath and metal be modeled as separate phases. They investigated the effect of anode gaps on the central channel width in the transverse direction. They found that reducing the gap caused large bath-metal interface fluctuations. The flow-induced magnetic field and the electric current did not affect the interface deformation significantly toward the center of the cell; however, the deformation was affected toward the sides.

1.2.3 Discrete Particle Model (DPM)

Liu (Liu, et al., 2019) studied the evolution and concentration distribution of undissolved alumina particles in a smelting cell caused by the CO_2 bubble-driven bath flow. They modeled the undissolved alumina particles using DPM and bath flow resulting from bubbles using VOF. They found that the concentration of alumina particles is lowest in the central channel compared to the side channels and the ACD space. Moreover, they observed that the alumina gradient in the transverse direction was larger than in the longitudinal direction. The simulation indicated that a physical time of approximately 20 min was required for the alumina concentration to reach a steady state.

1.2.4 Large-Eddy Simulation (LES)

Baiteche et al. (Baiteche, et al., 2017) performed a large-eddy simulation (LES) study of a smelting cell using a VOF model with two phases—bath, metal—and they studied the flow vortices inside the cell at the bath-metal interface. They concluded that the LES model provided a faithful representation of the small eddies and their impact on the overall flow, which was not provided by the Reynolds-averaged

Navier-Stokes (RANS) approach using the k-epsilon turbulence model. It can be inferred from their study that the flow predictions are nearly unaffected by choice of subgrid-scale viscosity models.

1.3 PROPOSED APPROACH

The literature review shows that most CFD simulation efforts have not modeled or studied most of the coupled multiple physics involved in a smelting process or their simultaneous interactions during operation. Therefore, in this effort, a CFD RANS model was developed and verified (see Section 3.1), which captures aluminum dissolution, diffusion, and consumption, along with electromagnetics and CO_2 release from the anode. Section 3.1 presents a basic framework for the CFD study of the smelting process using the open-source tool OpenFOAM-v8 (Welle, et al., 1998), which can later be extended to more complex smelting process simulations. The preliminary results obtained from the CFD model on a single anode-cathode cell are reported, and the coupled qualitative behavior of different flow physics are assessed.

Low-fidelity RANS models are predominantly described in the literature as being used to study the smelting process. However, the flow in a smelting process is highly transient, so the RANS models cannot fully represent the flow. Therefore, Section 3.2 describes an extension of the RANS model to an LES model. A detailed investigation of the characteristics of the large-scale flow oscillations induced by the bubbles and the electromagnetic forces in a conventional large-scale smelter was performed. The evolution of dissolved alumina in the bath and the bath temperature distribution in the smelter are addressed.

2. BENEFITS TO THE FUNDING DOE OFFICE'S MISSION

The Advanced Manufacturing Office (AMO) funded this collaboration under the purview of the Office of Energy Efficiency and Renewable Energy (EERE) at the US Department of Energy (DOE) through the High-Performance Computing for Energy Innovation (HPC4EI) umbrella program. The underlying objective of the program is to identify, address, diagnose, and resolve unique challenges to large-scale manufacturing processes which are directly proposed to reduce chemical emissions, improve the energy efficiency of operations, and/or provide an optimal yield of the desired product. The value proposition for the collaborators arises from a combination of multiphysics computational tools executed to maximize the strengths of each tool on HPC resources hosted at DOE's national laboratories, to provide a thorough understanding of multiphysics phenomena in manufacturing operations, and to inform possible improvements to crucial process parameters.

In support of DOE's mission to grow the American economy, implement process development, and enhance the energy efficiency of manufacturing operations, this collaboration between Alcoa USA and Oak Ridge National Laboratory (ORNL) accomplished the following objectives using HPC resources at ORNL and the National Renewable Energy Laboratory (NREL) Eagle Computing System:

- established a methodical flow of process information from Alcoa to ORNL pertinent to aluminum smelting technology

- calibrated an open-source computational tool, OpenFOAM, to resolve all spatio-temporal scales of *modeled* turbulence, electromagnetics, dissolution of solids in a molten electrolyte (cryolite), and diffusion of carbon-containing gases to the emissions profile, as observed in Alcoa's proprietary smelting technology

- acquired time-accurate prediction of greenhouse gas emissions in Alcoa's proprietary smelting technology

- acquired time-accurate and time-averaged resolution of inertial turbulence in Alcoa's proprietary smelting cells using the LES model in OpenFOAM, with sub-models for resolution of eddies smaller than the smallest grid element; successfully implemented layers of multiphysics models for Alcoa to readily adopt and validate with measured data from manufacturing operations

- sought optimum location of the feeders through the LES turbulence flow map that can enable efficient thermoelectric balance, reduce the risk of short circuits in the cell array, and prevent "mucking" or accumulation of charge material over the cathodes of smelting cells

This endeavor furthers the current state-of-the-art of aluminum smelting processes by acquiring multiphysics data at the scale of detail that can be provided by HPC resources, which are infeasible and impractical to obtain through physical field tests alone.

3. TECHNICAL DISCUSSION OF WORK PERFORMED BY ALL PARTIES

3.1 PRELIMINARY CFD MODEL DEVELOPMENT, VERIFICATION, AND PREDICTIONS

This section discusses the RANS CFD model developed to simulate the smelting process and the limited verification and validation performed for the developed model before it was extended to perform a high-fidelity transient LES study of an industrial scale smelter (Section 1.2.4).

The computational modeling of the flow physics inside the electrolytic cell is performed based on an Eulerian-Eulerian multifluid approach (Drew , et al., 2006). Although the multifluid approach is challenging in terms of obtaining a mesh-converged solution (Panicker, et al., 2018), it is widely used for CFD modeling and study ((Feng, et al., 2011) (Einarsrud, et al., 2017) (Liu, et al., 2019) (Eick, et al., 2015)) of smelting process because of its ability to provide a computationally inexpensive solution. The multifluid model is derived by averaging the instantaneous flow equations that are valid for micro-scale flow features. Therefore, the multifluid model approach captures the mesoscale features of the flow as explained by Panicker et al. (Panicker, et al., 2020). The micro-scale effects for mass, momentum and heat transfer across phases come through the interphase submodels for species, $S_{i,\,bath}$, in Eq. (4); momentum, $F_{D,}$ in Eq. (2); and energy, Q_I, in Eq. (3). The submodels used in the multifluid equations to study smelting are given in Table 1. The governing equations for thermal, mass, and momentum evolution for the bath, alumina, and CO_2 phases are provided below.

Continuity

$$\frac{\partial \rho_\phi \alpha_\phi}{\partial t} + \nabla \cdot \rho_\phi \alpha_\phi u_\phi = S_\phi \tag{1}$$

Momentum

$$\frac{\partial \rho_\phi \alpha_\phi u_\phi}{\partial t} + \nabla \cdot \rho_\phi \alpha_\phi u_\phi u_\phi = -\alpha_\phi \nabla p_l + \nabla \cdot \boldsymbol{\tau}_\phi + \rho_\phi \alpha_\phi \boldsymbol{g} + \boldsymbol{F_D} + \boldsymbol{L_{bath}} \tag{2}$$

Energy

$$\frac{\partial \rho_\phi C_{p\phi} \alpha_\phi T_\phi}{\partial t} + \nabla \cdot \rho_\phi C_{p\phi} \alpha_\phi u_\phi T_\phi = \nabla \cdot \alpha_\phi k_{\phi eff} \nabla T_\phi + Q_I + HD \tag{3}$$

Species

$$\frac{\partial \rho_\phi Y_{i,\,bath}}{\partial t} + \nabla \cdot \alpha_{bath} u_{bath} Y_{i,\,bath} = \nabla \cdot D_{eff,\,bath} \nabla Y_\phi + I_I + S_{i,\,bath} \tag{4}$$

Voltage

$$\nabla \cdot \sigma \nabla V = 0 \tag{5}$$

Magnetic field

$$\nabla \times \boldsymbol{B} = \mu_0 J \tag{6}$$

$$\boldsymbol{B} = \nabla \times \boldsymbol{A} \tag{7}$$

Turbulence

$$\frac{\partial \alpha_{bath} k_{bath}}{\partial t} + \nabla \cdot \alpha_{bath} u_{bath} k_{bath} = \nabla \cdot \nu_{eff,\,bath} \nabla k_{bath} + P - \varepsilon \tag{8}$$

$$\frac{\partial \alpha_{\text{bath}} \varepsilon_{\text{bath}}}{\partial t} + \nabla \cdot \alpha_{\text{bath}} u_{\text{bath}} \varepsilon_{\text{bath}} = \nabla \cdot \nu_{\text{eff, bath}} \nabla \varepsilon_{\text{bath}} + C_{1\varepsilon} \frac{\varepsilon_{\text{bath}}}{k_{\text{bath}}} P - C_{2\varepsilon} \frac{{\varepsilon_{\text{bath}}}^2}{k_{\text{bath}}}, \quad (9)$$

where

$\nu_{\text{eff}} = \nu_{\text{lam}} + \nu_{\text{T}}$, $\nu_{\text{T}} = C_{\mu} \frac{{k_{\text{bath}}}^2}{\varepsilon_{\text{bath}}}$, $C_{\mu} = 0.09$, $C_{1\varepsilon} = 1.44$, $C_{1\varepsilon} = 1.92$,

$\boldsymbol{\tau}_{\phi} = \alpha_{\phi} \mu_{\phi\text{eff}} \left[\nabla u_{\phi} + \left(\nabla u_{\phi} \right)^T - \frac{2}{3} \left(\nabla \cdot u_{\phi} \right) I \right]$

$\mu_{\phi\text{eff}} = \mu_{\text{lam}} + \mu_{\text{sgs}}$,

$k_{\phi\text{eff}} = k_{\text{lam}} + k_T$

$\text{D}_{\text{eff, bath}} = \text{D}_{\text{lam}} + \text{D}_{\text{sgs}}$,

HD - the heat of dissolution of alumina,

i - cryolite, alumina,

$S_{i,bath}$ − sources and sinks caused by electrochemical reactions in the bath on the anode,

phases, ϕ - solid alumina, bath, and CO_2 gas, and

$\boldsymbol{L_{\text{bath}}} = \boldsymbol{J} \times \boldsymbol{B}$, where $\boldsymbol{J}$ is electric current density and $\boldsymbol{B}$ is the magnetic field

Table 1. Interphase models for momentum, mass, and heat exchange used in the multifluid model

Interphase models	Model
F_{D} Schiller Naumann	$\alpha_{\text{d}} \rho_{\text{bath}} C_{\text{D}} \lvert u_d - u_{bath} \rvert (u_d - u_{bath})$ $C_{\text{D}} = \frac{24}{Re_{\text{d}}} (1 + 0.15 Re_{\text{d}}^{0.687})$ Re_{d} – Reynolds number based on dispersed phases: alumina solid or CO_2 gas bubble
Q_{I} Ranz-Marshall	$K(T_{\text{solid}} - T_{\text{bath}})$ $\text{K} = \frac{6 \alpha_s k_{\text{bath}} \text{Nu}}{d_{\text{p}}^2}$ $Nu = 2 + 0.6 Re_{\text{s}}^{1/2} Pr^{1/3}$ $\text{Re}_{\text{s}} = \frac{d_{\text{p}} \rho_{bath} \lvert \mathbf{u}_s - u_{bath} \rvert}{\mu_{bath}}$ $\text{Pr} = \frac{C_p \mu_{\text{bath}}}{k_{\text{bath}}}$
I_{I} Frossling	$K\left(Y_{\text{solid, al}} - Y_{\text{bath, al}}\right)$ $\text{K} = \frac{6 \alpha_s D_{al,bath} Sh \rho_{bath}}{d_{\text{p}}^2}$ $Sh = 2 + 0.552 Re_{\text{s}}^{1/2} Sc^{1/3}$, $\text{Sc} = \frac{\mu_{\text{bath}}}{\rho_{\text{bath}} \text{D}_{\text{al,bath}}}$

Although the multifluid approach can simulate large systems with considerably low computational cost compared to other multiphase CFD approaches (e.g., Volume of Fluid, level set, and Eulerian-Lagrangian), it is still costly to model a smelter with multiple phases and associated interactions. Therefore, only three phases corresponding to CO_2, Al_2O_3 powder, and cryolite bath were considered in the study. The fourth phase corresponding to the molten aluminum pool settled on the cathode is not currently considered due to computational challenges in terms of cost and convergence. Besides, the first step of this CFD modeling effort is to study the mixing inside the bath from CO_2 and MHD and its impact on alumina distribution. At this stage, liquid aluminum metal pad and its impact on alumina dissolution and mixing is ignored. The drag model used in this work is from Naumann and Schiller (Naumann, et al., 1935), which is reasonable for the small bubble size (2 mm) considered in this study (Portuousi, et al., 2014). The alumina fed into the cell dissolves and diffuses inside the cell. The diffusion of the alumina species is modeled using the species transport equation, and the dissolution is modeled as a phase transfer from the alumina powder phase to the bath phase using the Frossling model (Frossling, 1938) given in Table 1. The injected alumina particle size is assumed to be constant in the current work, although it shrinks while dissolution progresses. This controls the number of undissolved particles that settle to the bottom of the bath and eventually pass into the settled aluminum pool.

The particle size distribution evolution can be accounted for using the population balance equation. In future efforts, the goal is to couple the population balance with the existing framework to predict such effects. The turbulence caused by various effects like bubble agitation and MHD is captured using the standard k-epsilon model, which is computationally cheap and tractable. A more sophisticated multiphase k-epsilon model that would account for multiphase interactions with low computational cost can be found in Fox (Fox R. O., 2014); these models capture turbulence production as a result of the other phases directly in the turbulence model. The heat transfer between the alumina solid and the bath is accounted for by the Ranz-Marshall model (Ranz, 1952), which can be used to limit the low solids fraction as observed in the current study (Mankad, et al., 1997). Two main heat transfer mechanisms cause the temperature variations in the bath: (1) sensible heat lost to heat the alumina particles entering at room temperature, and (2) the heat of dissolution (HD) used by the alumina to dissolve in the bath. Equation (3) gives the thermal energy evolution, which accounts only for the first mechanism through the Ranz-Marshall model. The second mechanism must be captured using the HD model discussed in the LES modeling and simulation section below.

3.1.1 Electromagnetics

The electric current passing from anode to cathode through the molten bath controls the alumina consumption, CO_2 production, and aluminum production. Moreover, the electricity produces a magnetic field around the bath which then interacts with the current to produce the Lorentz force, causing MHD predominantly in the space between the anode and the cathode. The current density across the electrolytic cell is predicted by solving the voltage equation (Severo, et al., 2005). The voltage across the cell has several components: ohmic voltage, decomposition voltage, over-voltage, and bubble voltage. The ohmic voltage drop occurs across the solids (anode, cathode) and the bath; the decomposition voltage drop occurs across the aluminum pool settled, the over-voltage drop occurs on the anode and cathode, and the bubble voltage occurs across the CO_2 accumulation layer on the anode. However, only the ohmic voltage across the cell is considered when predicting electric current density. The calculated current density is fed to the magnetic vector potential equation, Eq. (7), to compute the magnetic field. The Lorentz force is computed from the magnetic field and electric current density prediction from Eqs. 5–7 and is added to the bath phase momentum to predict the MHD effect in the cell.

3.1.2 Electrochemical Reactions

The solver, which is based on the multifluid approach in OpenFOAM, cannot simulate surface reactions. Therefore, electrochemical reactions were modeled by adding source terms for the production of CO_2 and sink terms for the production of alumina consumption. These terms are added to their respective species and phase transport equations. A similar modeling strategy can be found in Li et al. (Li, et al., 2011) and Zhang et al. (Zhang, et al., 2014). The source terms are only active on the boundary cells next to the anode's surface.

The amount of CO_2 produced, and the amount of alumina consumed in the anode are determined by the electrochemical reactions taking place on the anode, as shown below:

$$2Al_2OF_6^{2-} + 4F^- + C \xrightarrow{yields} 4AlF_4^{2-} + CO_2 + 4e^- \quad (10)$$

$$2Al_2O_3 + 3C \xrightarrow{yields} 4Al + 3CO_2. \quad (11)$$

The electrochemical reactions indicate that 4 moles of electrons are produced per mole of CO_2. The current density on the anode's surface, which is determined from the solution of the voltage equation, will provide the number of electrons passing across the anode per unit area in 1s, which can be used to determine the CO_2 produced ($\mathbf{S_{co2}}$) in the cells next to the anode surface. Similarly, alumina consumption $\mathbf{S_{Al2O3}}$ can be estimated. Not all the current supplied is utilized for CO_2 production in a typical smelter. Some of the current is lost in the back reaction of dissolved aluminum to alumina in the presence of oxygen. Thus, a CE factor (η) must be added before the magnitude of current density (J). For this work, it is assumed to be 1.

$$S_{CO2}\ (kg/m^3 s)\ = \frac{(\eta|\boldsymbol{J}_{cell}|\boldsymbol{A}_{cell})MW_{CO_2}}{6FV_{cell}}$$

$$(12)S_{Al_2O_3}\ (kg/m^3 s)\ = -\frac{(\eta|\boldsymbol{J}_{cell}|\boldsymbol{A}_{cell})MW_{Al_2O_3}}{4FV_{cell}} \quad (13)$$

The amount of aluminum that has settled on the cathode is not explicitly captured in the simulation. However, as shown below, quantitative estimates on the aluminum produced on the cathode can be based on the predicted current passing through the cathode:

$$\text{Net aluminum produced on the cathode (kg/s)} = \frac{(\int \eta|\boldsymbol{J}_{cell}|\boldsymbol{dA}_{cell,cathode})MW_{Al}}{3F} \quad (14)$$

Figure 2 provides a quick summary of the capabilities added to the existing multifluid model-based solver of OpenFOAM. Note that the CFD modeling strategy discussed and the capabilities added to OpenFOAM are applicable not only for smelting but also for other processes such as H_2 and lithium production involving electrolysis.

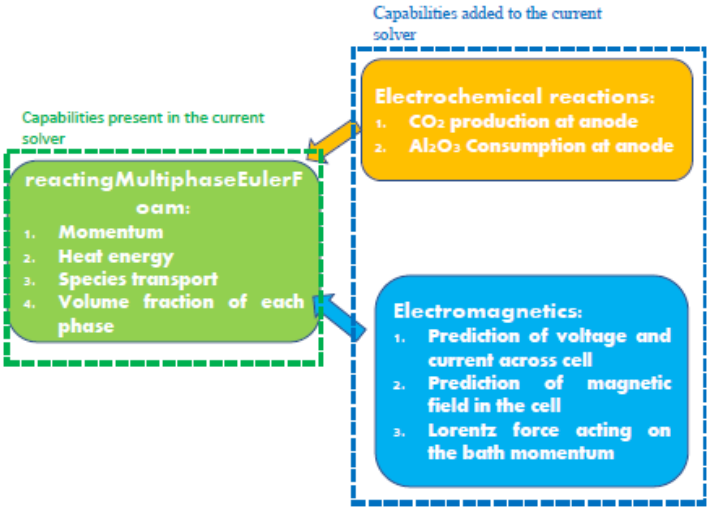

Figure 2. Overview of the physics added to the existing solver to capture flow, mass, and heat transfer in an electrolytic cell.

3.1.3 Simulation Setup

The focus of this section is to describe testing of the predictive capability of the RANS model before it was extended to an LES model capable of simulating an industrial-scale smelter. Therefore, to avoid the complexities introduced by the industrial-scale geometry, a single anode-cathode unit cell was considered for model testing. The computer-aided design (CAD) model for the single anode-cathode unit cell,

including the dimensions of the anode, the cathode, and the feeder, is shown on the left in Figure 3. On the right, the mesh cut section of the cell is illustrated. Two prism layers are inserted on the cell walls to capture the steep velocity gradients on the boundary. Approximately 100,000 15 mm mesh elements were used to study the behavior of different physics incorporated into the CFD model. The flow, electrical properties, and boundary conditions (BCs) used in the simulation are reported in Table 2,

Table 3, and

Table 4, respectively. The numerical schemes used in the study are second-order in space and first-order in time. A second-order time scheme was used for second-order accuracy. However, the smelting process involves the complex coupling of multiphysics, and the second-order time scheme was causing solution divergence. Hence, a first-order time scheme was adopted for the current study. The simulation was run on 24 cores for 3 days with a time step of 1 ms to achieve 160 s of cell operation time. The time-averaged simulation results obtained at 160 s are reported in the results section.

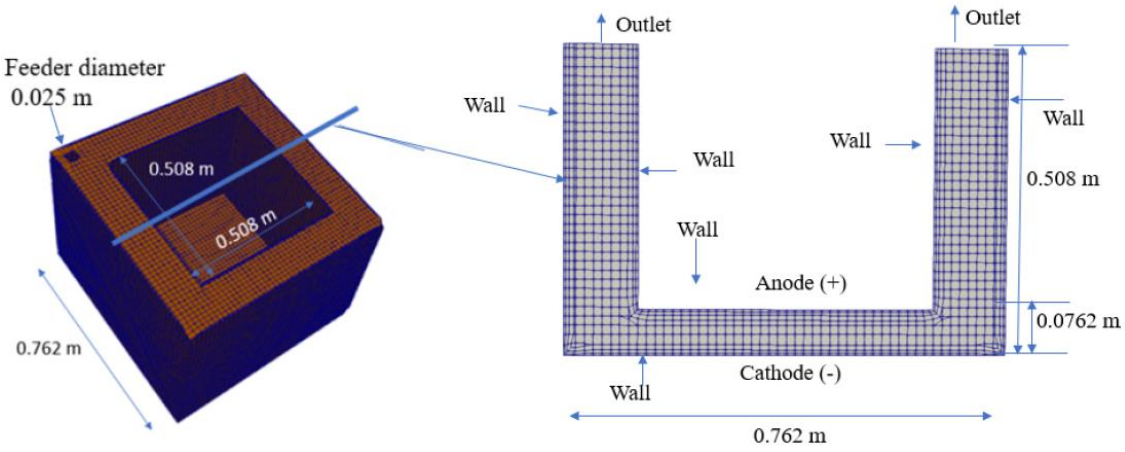

Figure 3. Geometric dimensions and representative view of mesh.

Table 2. Thermophysical properties of phases

Properties	**Liquid phase: bath**	**Solid-phase: alumina**	**Gaseous phase: CO_2**
$\rho\ (kg/m^3)$	2,050	3,950	1.98
$\mu\ (Pa\ -\ s\ )$	0.0025	0.1	1.4e-5
$D\ (m^2/s^2)$	1.5e-9	-	-
Y_i (-)	0.9736	0.0264	0
C_p (J/kg-K)	1,850	880	846
$k\ (W/\mathrm{m}-\mathrm{K})$	0.5	25	0.025
$d_p\ (m)$	-	1e-4	0.002
MW (g/mol)	209	101	44
S (-)	-	0.08	-

Table 3. Electric properties of the cell

Properties	**Value**

σ (S)	280
μ_0 (H/m)	1e-6
Voltage (V)	2.5

Table 4. BCs used in OpenFOAM.

BC	Walls	Outlet	Anode	Cathode
Bath phase velocity	No slip	Free slip	No slip	No slip
Alumina phase velocity	No slip	Free slip	No slip	No slip
CO_2 gas phase velocity	No slip	Degassing	No slip	No slip
Species	Zero gradient	Zero gradient	Zero gradient	Zero gradient
Voltage	Zero gradient	Zero gradient	Fixed value	Fixed value
Magnetic field	Zero gradient	Zero gradient	Zero gradient	Zero gradient
Volume fraction	Zero gradient	Zero gradient	Zero gradient	Zero gradient
Turbulence	Wall function	Wall function	Wall function	Wall function

3.1.4 Limited Verification of the CFD Model

A series of verification studies were performed to verify the crucial smelting physics predicted by the CFD model. Because of the lack of availability of experimental data, several physics predicted by the CFD model were verified using the method of manufactured solution, and the remaining were verified through analysis of experimental data.

3.1.4.1 Diffusion of alumina

The diffusion of alumina was modeled by its transport as a species, and predictions from the simulation were validated against the experiment performed by Skybakmoen et al. (Skybakmoen, et al., 1997). In the experiment, a disk of solid alumina was submerged in a pool of cryolite, and the sphere was rotated using a shaft. The rotational motion caused dissolution and diffusion of alumina in the cryolite bath, after which the mass fraction of dissolved alumina was monitored in time. The evolution profiles of the mass fraction of dissolved alumina as predicted by CFD, the analytical solution, and as measured in the experiment, are given in Figure 4. Results indicate that the dissolution predicted by the CFD model matches reasonably well with the dissolution experiment.

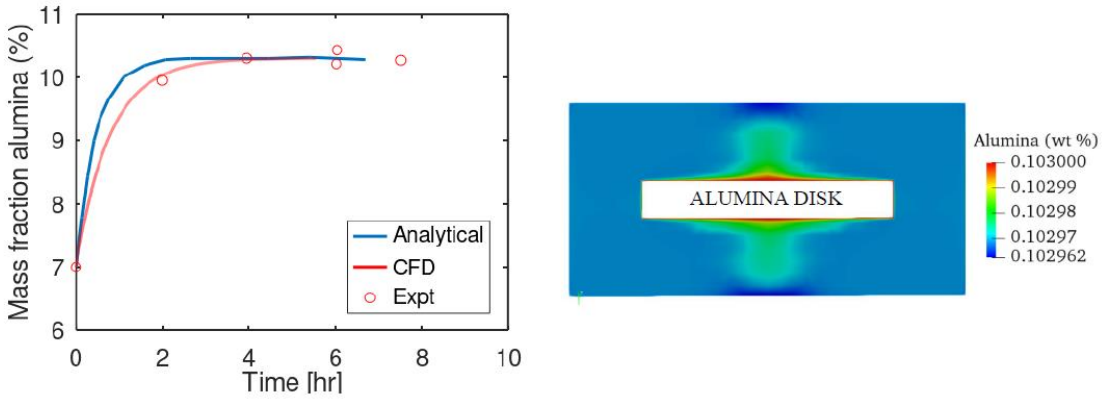

Figure 4. Time evolution of alumina's mass fraction in bath (left) and mass fraction contour after t = 5.55h at saturation (right).

3.1.4.2 Dissolution of alumina

The correct behavior of the alumina dissolution model used in the CFD model was tested by monitoring the evolution of the volume-averaged dissolved alumina fraction in the cell with time (Figure 5). At a steady state, the dissolution should stop, and the dissolved mass fraction of alumina should attain a value close to the solubility and should then remain unchanged. Two different solubility limits—8% by wt. and 3% by wt.—were used to test the dissolution model. The time evolution of dissolved alumina mass fraction for these solubilities is given in Figure 5, which shows that at a steady-state, the volume-averaged mass fractions of alumina attain their respective solubilities of 8 and 3% and remain unchanged, which verifies the correct behavior of the dissolution model adopted.

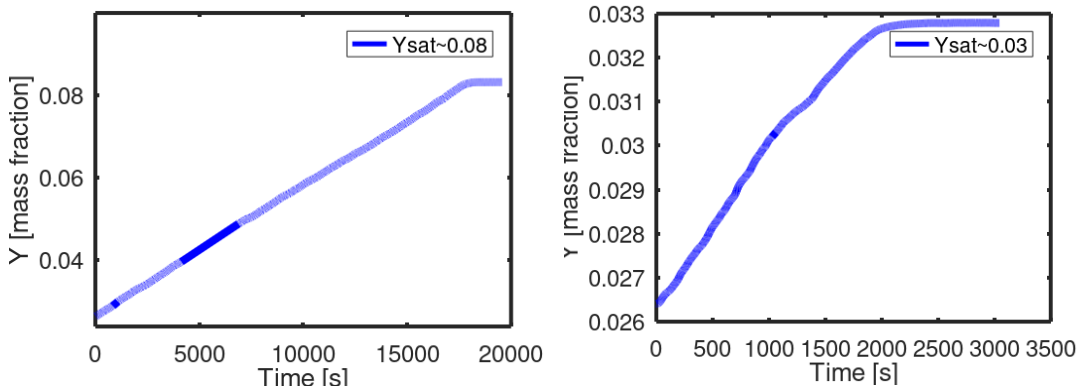

Figure 5. Volume-averaged mass fraction of alumina vs. time for Ysat (saturated unit weight) ~ 0.08 (left) and Ysat ~ 0.03 (right).

3.1.4.3 Plume profile from CO_2 bubbles

The image on the left in Figure 6 shows the volume fraction profile of the CO_2 gas plume in red as predicted by the simulation compared. The plume profile follows the trend predicted by Zhao et al. (Zhao, et al., 2017). The image on the right shows the CO_2 gas-driven bath flow. Bath flow predicted by the simulation (circled in red) follows the trend predicted by Zhao et al. (Zhao, et al., 2017).

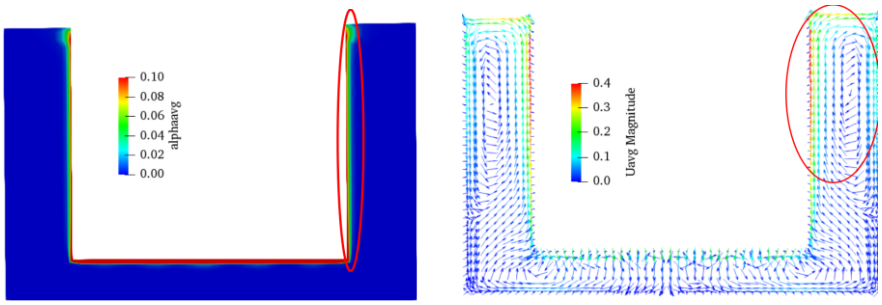

Figure 6. CO_2 bubble plume profile (left) and CO_2-driven flow (no MHD) (right).

3.1.4.4 Flow profiles in the bath

The gas-induced bath flow was verified against the particle image velocimetry (PIV) flow experiment (Feng, et al., 2006). Because of the various challenges involved in performing a flow experiment of an exact smelting cell with cryolite and CO_2 as working fluids, in this experiment, air and water were used as working fluids. Air was injected from the bottom of the anode in the experiment to replicate the CO_2 production resulting from an electrochemical reaction. The flow circulations generated by the air bubbles predicted by CFD on different planes (A and B) are shown in Figure 7 and Figure 8. The flow circulation trends predicted by CFD for measurement planes A and B appear to be like PIV (Feng, et al., 2006). However, the center of the circulations is not the same. Note that in the experiment, the air was injected from the bottom of the anode to replicate the production of CO_2 from electrochemical reactions. However, in the CFD, the air nucleates from the bottom of the anode. The discrepancy in the results could be attributed to the difference in methods adopted to generate air bubbles in the cell.

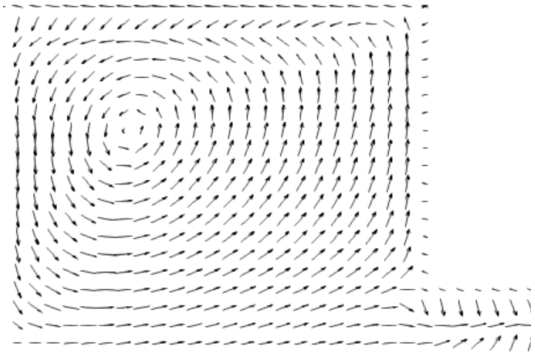

Figure 7. Velocity vector from CFD at location A.

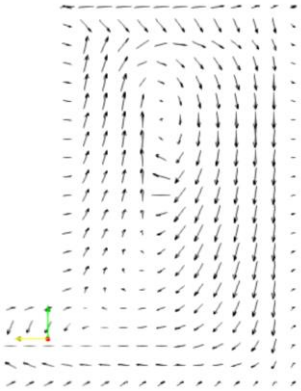

Figure 8. Velocity vector from CFD at location B.

3.1.4.5 Heat of dissolution

Alumina was injected into an adiabatic cylindrical container with a pool of cryolite bath maintained at a bath temperature of 950°C, as shown in Figure 9 (right), and the alumina was allowed to fully dissolve into the bath. The injection was stopped at 1 s to ensure that only 1 g of alumina entered the bath. The CFD prediction of the bath temperature drops with time, whereas dissolution is reported as shown in Figure 9 (left). Upon complete dissolution, the final temperature attained by the cryolite bath for the HD =820 KJ/kg of alumina was calculated by performing a thermal energy balance on the system. The final temperature obtained from the energy balance calculation and CFD prediction are reported in Table 5. The negligible difference in temperature predicted by CFD and analytical calculation verifies the correct behavior of the HD model.

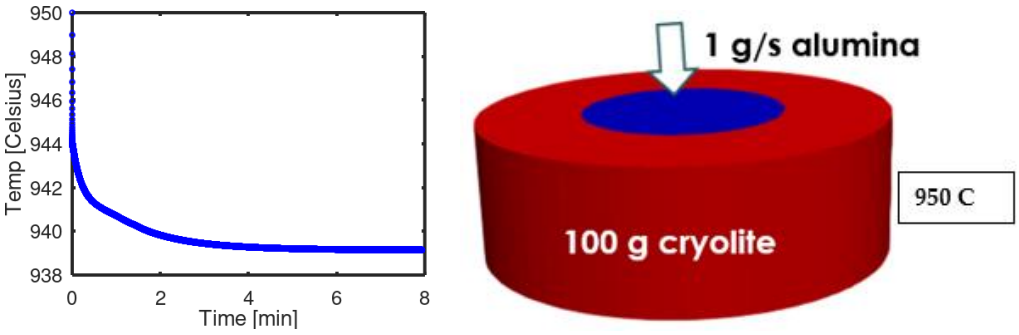

Figure 9. Bath temperature cooling (left) and geometry (right) considered for verification of HD.

Table 5. Predictions of bath temperature at steady state

	CFD (℃)	Analytical prediction (℃)	Error
Final bath temperature	939.5	941	0.1 %

3.1.4.6 Electric current

The CFD prediction of electric current was verified by comparing it with the current calculated from Ohm's law for a thin cylindrical conductor, as shown in the image on the left of Figure 10. The current distribution predicted by the CFD voltage potential equation, as shown on the right in Figure 10, was integrated over the cross-sectional area to obtain the total current passing through the conductor. The total current predicted by CFD is in close agreement with the total current calculated from Ohm's law, as shown in Figure 10.

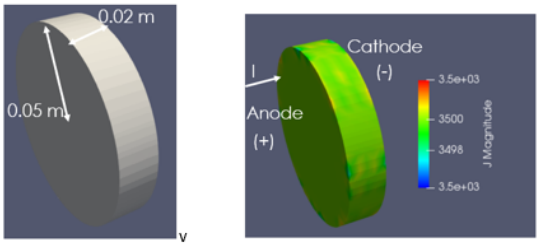

I = V/R

Where, R = L/(Cond*A)

V= 25 V

Cond = 2.8 S/m

A = pi*0.05*0.05

L = 0.02 m

I_CFD = 27.438 A

I_ohms_law = 27.489 A

Figure 10. The geometry of the cylindrical conductor (left) and current distribution (right), along with current predictions from the Ohm's law and CFD.

3.1.4.7 Mesh dependency

A limited study was performed on mesh dependence over time-averaged bath velocity driven by buoyant bubbles of CO_2 to quantify the numerical error associated with the mesh used to complete the exploratory simulations. Figure 11 shows the bath velocity comparison for the current mesh size and a mesh size of half the current mesh size. The comparison shows that the peak bath velocity is slightly lower for refined mesh than for coarse mesh; however, the circulation patterns of both meshes have similar profiles, indicating that the numerical error associated with the current mesh is insignificant. However, the comparison between different meshes is only performed for gas-driven flow by switching off the other effects such as MHD, alumina dissolution, and heat transfer.

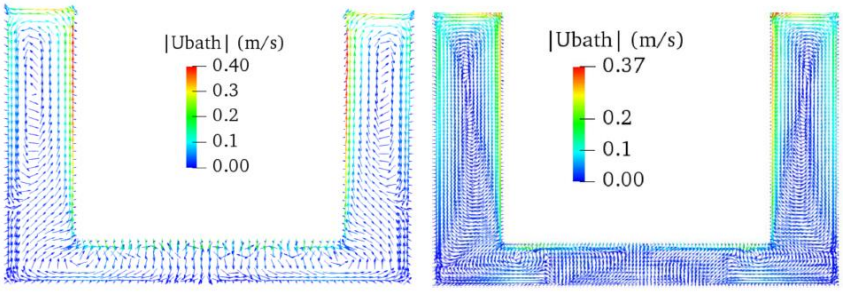

(a) Mesh size = 15 mm (b) Mesh size = 7.5 mm

Figure 11. Velocity dependence on the mesh.

3.1.5 CFD Predictions on a Unit Cell

3.1.5.2 Electromagnetics

The current path and magnitude flowing from anode to cathode when the electrolytic cell is subjected to a voltage of 2.5 V are shown in Figure 12. The average current density predicted from the simulation shows approximately 9,000 A/m^2 passing through the anode, which corresponds to a total current of approximately 2,600 A. This prediction correlates with the typical total current supplied to a unit's electrolytic cell used for the smelting process. The current from anode to cathode emanates a magnetic field. Figure 13 is a cross-section taken parallel to the anode-cathode in the anode-cathode gap showing

the magnetic field produced by the current. The direction of the magnetic field is clockwise, which is consistent with the righthand rule applied to determine the direction of the magnetic field produced by a passing electric current. The magnetic field produced by the electric current interacts with the electric current to produce the Lorentz force, as shown in Figure 13 (bottom left). The Lorentz force is directed toward the middle of the anode. The Lorentz force acts on the fluid, including the electrolyte and aluminum metal pad between the anode-cathode space, pushing the fluid toward the center to produce an MHD metal pad heave (Severo, et al., 2005). The velocity vector plot presented in Figure 13 (bottom right) shows the complex flow pattern induced by MHD.

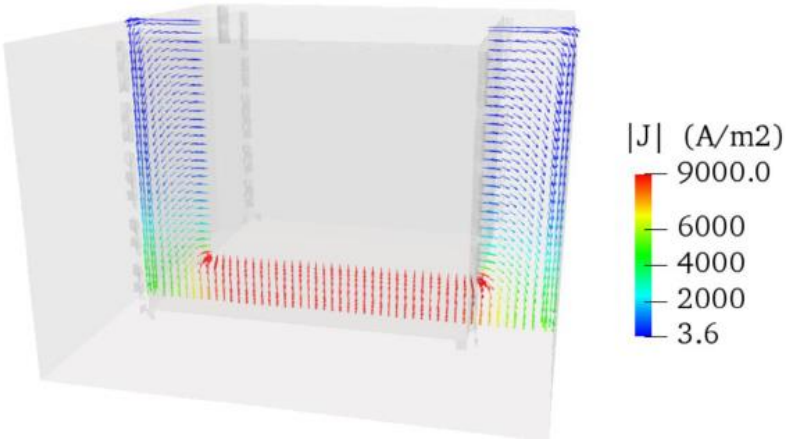

Figure 12. A vector plot of electric current on a central axial plane of the anode.

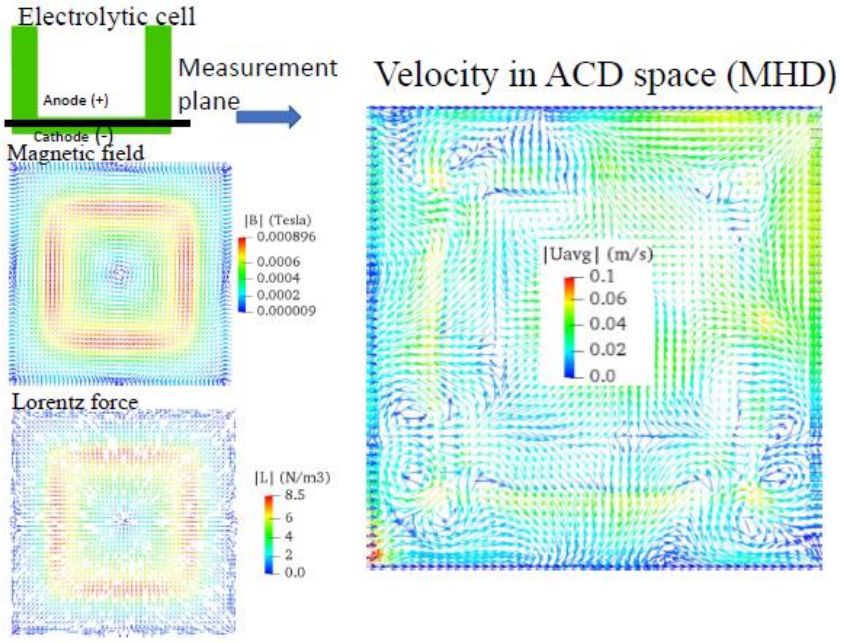

Figure 13. Magnetic field, Lorentz force, generated from electric current and MHD.

3.1.5.3 Dissolution and consumption of alumina

Figure 14 shows the undissolved solids fraction and mass fraction of dissolved alumina in the bath, respectively, on a plane cutting the injector. The initial mass fractions of cryolite and alumina used in the simulation were 0.9736 and 0.0264, respectively, as commonly found in a conventional smelter cell. The

alumina was injected through a point feeder with a mass flow rate of 4.62e-4 kg/s such that it compensates for the net alumina consumed in the anode. To achieve a better numerical convergence, both alumina injection and consumption were turned on only after 70 s of the simulation time. The undissolved alumina powder was dispersed in the bath as a result of the CO_2 bubble-driven recirculation. The undissolved alumina dispersed in the bath continuously dissolved, explaining the correlation between the undissolved alumina volume fraction and the dissolved alumina mass fraction. The simulation was started with an initial bath alumina mass fraction of 0.0264. As seen in Figure 15, the mass fraction dropped below 0.0264 on the right side as a result of the consumption of alumina at the anode. The alumina feeder was placed close to the plane's left side, making the bath alumina rich on the left side, as seen in Figure 15. The red spot of the alumina mass fraction seen on the bottom left corner of the plane was caused by the increased concentration of undissolved alumina solid accumulated in that region, which eventually dissolved.

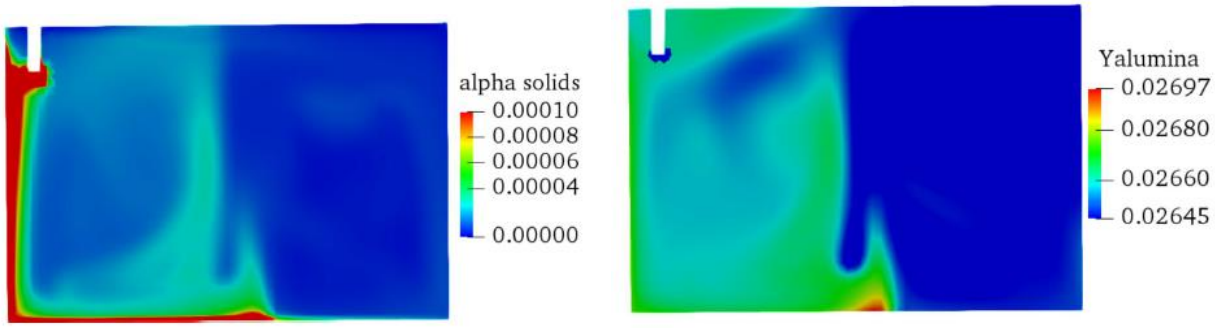

Figure 14. Undissolved solids (left) and mass fraction of dissolved alumina (right) on an axial plane through the feeder.

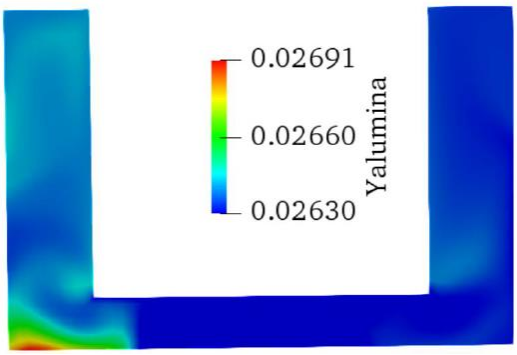

Figure 15. Mass fraction of dissolved alumina on an axial plane through the anode.

3.2 LARGE-EDDY SIMULATION (LES) OF THE SMELTING PROCESS IN A CONVENTIONAL SMELTER

3.2.4 LES Model for Smelting

This section discusses the LES model predictions of the smelting process in a conventional smelter. According to the literature, RANS models are predominantly used to study the multiphysics involved in the smelting process. The flow in a smelting process is highly transient, so the RANS models cannot fully represent the flow. Therefore, in this section, the RANS model presented in Section 3.1 is extended to perform high-fidelity LES flow simulations in an industrial-scale smelter.

The RANS model based on the multifluid approach was used as described in the previous section to perform low-fidelity RANS simulations of a unit cell. However, the applicability of the multifluid approach is not only restricted to RANS simulations. It can also be used for high-fidelity LES (Fox, 2012) (Panicker, et al., 2020) (Dhotre, et al., 2013). The LES model described in this section is an extended version of the RANS model discussed in the previous section. The turbulent viscosity used in the RANS model was replaced with the subgrid-scale Smagorinsky model to perform high-fidelity LES of smelting. Three phases—CO_2 bubble, alumina solid, and bath—were modeled, and the metal phase s not considered to reduce the complexity and computational time. The modeling details of electromagnetics and electrochemical reactions are given in the previous sub-sections of Section 3.1.

3.2.5 The Heat of Dissolution

The process of alumina dissolution from the solid to the liquid phase absorbs heat from the bath, causing bath temperature to drop. This drop in temperature can lead to the solidification of the bath, so it is critical to understand the impact of the HD on the temperature distribution of the bath. In this work, HD was modeled based on the dissolution rate of alumina, as given in Table 1 (Frossling).

$$H_D\ (J/m^3 s) = K\left(Y_{\text{solid, al}} - Y_{\text{bath, al}}\right) H_{per\ kg} \tag{15}$$

The heat of dissolution per kg (HperKg) of alumina dissolved is 820 kJ/kg and can be found in Table 2 (Thonstad, et al., 2016). HD was added as a volumetric heat sink term to the bath heat energy balance equation (Eq. 3).

3.2.6 Subgrid Model

Subgrid scale turbulent physics was accounted for using the well-established Smagorinsky model (Smagorinsky, 1963) used for LES studies. The formulation of the Smagorinsky model used by OpenFOAM is as below:

$$\nu_{\text{T}} = C_{\text{k}} \Delta \sqrt{k} \tag{16}$$

where

$\Delta = \sqrt[3]{\Delta V}$, V – the volume of the computational cell, C_{k}=0.094.

Turbulent kinetic energy (k) in Eq. (16) is obtained from the solution of the quadratic Eq. (17):

$$ak^2 + bk + c = 0 \tag{17}$$

$$a = \frac{C_{\text{e}}}{\Delta},\ C_{\text{e}}=1.048$$

$$\text{b} = \frac{2}{3}\text{tr}(\boldsymbol{D})$$

$$c = 2C_{\text{k}}\Delta(\text{dev}(\boldsymbol{D}) : \boldsymbol{D})$$

$$\boldsymbol{D} = \frac{1}{2}(\boldsymbol{\nabla} u + \boldsymbol{\nabla}(u)^T)$$

3.2.7 Modeling Turbulence Near Walls

A wall function is generally used to model the subgrid viscosity in the vicinity of the wall and is based on a universal wall law developed by Spalding (Spalding). This wall function law enables the modeling of turbulence near the wall for any wall y^+. The validity near-wall cell distance no longer depends on the wall y^+ value, but accurate prediction of turbulence in the boundary layer requires near-wall cell size, which provides a wall y^+<1. Such a resolution requires many cells, which will drastically increase the computational load, thus requiring a large number of processors and a considerable amount of simulation time. In this study, the resolution of cells near walls was not high, and the y^+value was greater than 30, in general, except in stagnated regions. The turbulence eddies generated in an electrolytic cell were primarily caused by the rising bubbles dragging the electrolyte and MHD, both of which can be considered as bulk effects at low Re numbers rather than wall effects. Therefore, shear-generated turbulence on the walls, as observed for a typical channel flow at a high Reynolds number, was absent. Hence, this study focused on the turbulent flow in the bulk of the electrolytic cell. The anodic diffusion layer is never attempted to be resolved due to the complexity caused by gas nucleation and significantly higher resolution requirements. Thus, this study will focus more on the bulk aspects of mass, momentum, and heat transport in an electrolytic cell.

3.2.8 Geometry and Mesh

The simulation was performed for a conventional smelter cell in the Alcoa manufacturing plant. This cell has 22 anodes in a row with a total of 44 anodes for two rows, as shown in Figure 16.

A faithful representation of the cell's dimensions is given in Figure 16Figure 16. This cell operates at a current of 175 kA, and the target current was achieved in the simulation by adjusting the voltage on each anode. Four feeders placed above the central channel were used to feed alumina in the simulation.

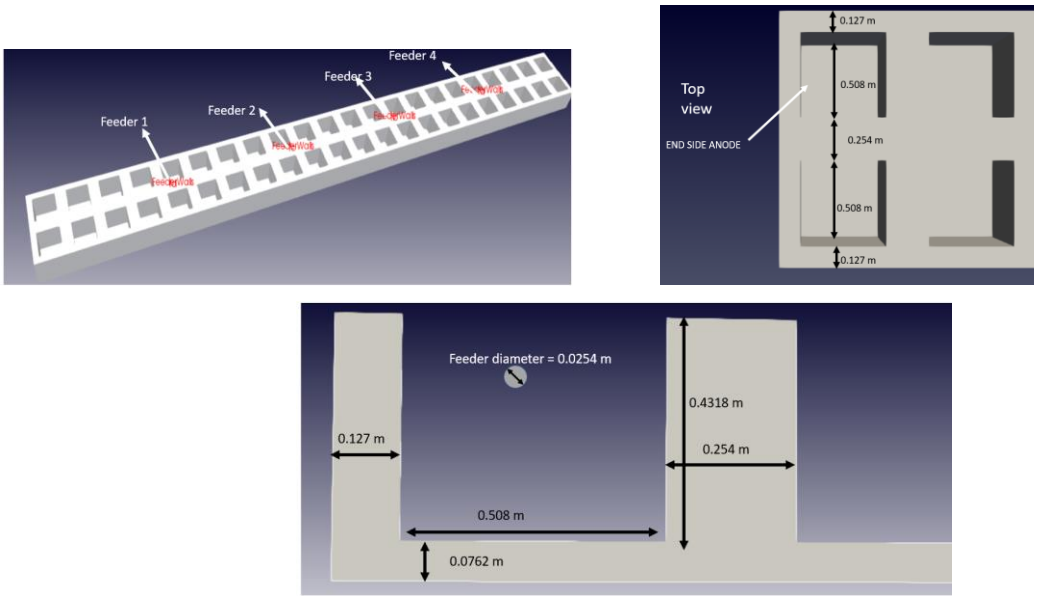

Figure 16. 22 × 2 anode array: geometry and dimensions.

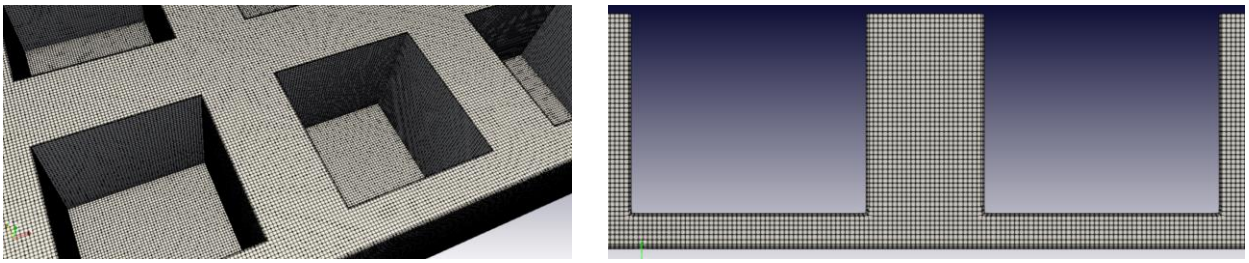

Figure 17. Representative views of the mesh on the 22 × 2 anode array.

Hexahedral elements with two prism layers were used for meshing the geometry, as shown in Figure 17. Approximately 10 million mesh elements were used to carry out the simulation. The bulk mesh size used is approximately 9 mm, and the near-wall boundary mesh sizes ranges from 3 – 4 mm.

3.2.9 Simulation Approach

The simulation was performed using the modified version of multiphaseEulerFoam in OpenFOAM-v8. Because the simulation was complex with multiple physics and prone to divergence, a procedure was followed to avoid divergence and improve simulation speed.

The simulation started with a time step of 0.5 ms and was later adjusted to 1 ms to improve the computational time. Similarly, the pressure tolerance at the start was fixed to 1e-14 and was later adjusted to 1e-12. The flow was first allowed to develop by only switching on the CO_2 production and switching off other smelting physics (MHD, Al_2O_3 consumption, and heat transfer) by adjusting the "maxIter" to 0 for species and energy in the "fvSolution" file of the solver. MHD was turned on after the flow-induced from CO_2 reached 20 s. Alumina was injected after 150 s, when the flow had reached a statistically stationary state, and the velocity, species mass fraction, and temperature were averaged for a sufficiently long time. The simulation required approximately 10 days to simulate 5 min of cell operation time with 560 processors. BCs, fluid and thermophysical properties, and initial conditions (ICs) for the simulation were retained from Panicker et al. (Panicker, et al., 2021).

3.2.10 CO_2: Nucleation of Bubbles and Evolution of Plume

The CO_2 gas bubbles are produced from the electrochemical reaction formed bubbles on the bottom and side surfaces of the conventional carbon anodes. The newly formed bubbles at the anode bottom pushed the older bubbles formed toward the periphery of the anodes. The bubbles that reached the edge of the anodes moved upward due to the density difference between the gas phase and the bath. The nucleated bubbles predicted by the simulation are shown in Figure 18. In this work, the nucleation of the bubbles was modeled by adding a mass source for CO_2 in the mass conservation equation of the gas phase. The gas fraction pattern at the bottom of the anode shows peaks and valleys, similar to those in the bubble nucleation observed for boiling applications. The excessive gas bubble accumulation at the bottom of the anode is not desired for efficient cell operation (Zhang, et al., 2013) (Alam, et al., 2003), because it forms a gas film that reduces the net electrical conductivity, leading to a higher Ohmic voltage drop, thus resulting in higher energy consumption. Moreover, the bubble motion beneath the anodes also introduces waves into the bath−metal interface, causing fluctuations.

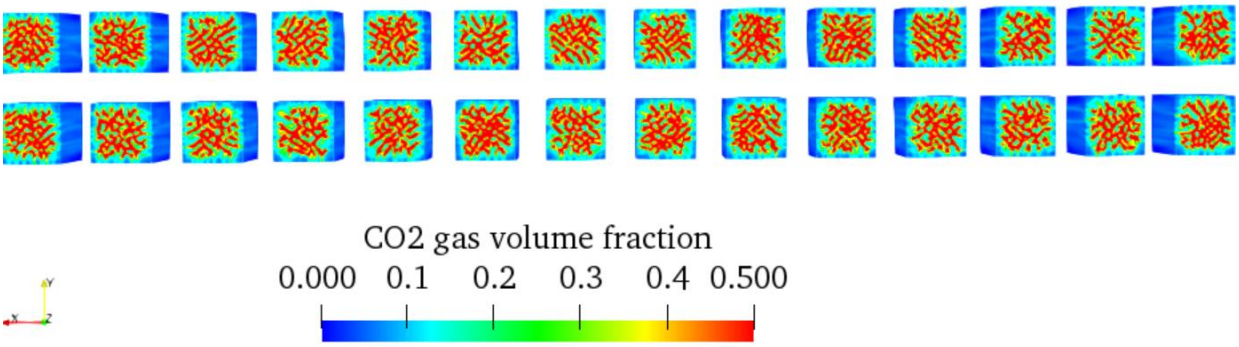

Figure 18. Gas nucleation at the bottom of the anodes.

The gas accumulation can be prevented using an inclined anode (Sun, et al., 2020), by smoothing the anode edges and using hydrophobic coatings. A basic horizontal anode with no smoothing and hydrophobicity was considered in this analysis. However, it is interesting to note that in Figure 18, the gas volume fraction at the anode bottom's periphery is significantly lower than the gas fraction toward the center of the anode bottom. It appears that the bath vortex formed at the periphery of each anode (refer to Figure 19) due to the interaction between the MHD forces and the bubble-induced forces, the gas bubbles at the periphery of the anode bottom towards sides of the anodes, causing the lower gas accumulation. Thus, gas accumulation can also be prevented by engineering bath flow patterns appropriately. For instance, if the vortex formed at the edges is elongated such that it spans from the center of the anode bottom to the periphery of the anode bottom, then gas accumulation can be prevented. This is perhaps may be achieved by tailoring the shape of the anode.

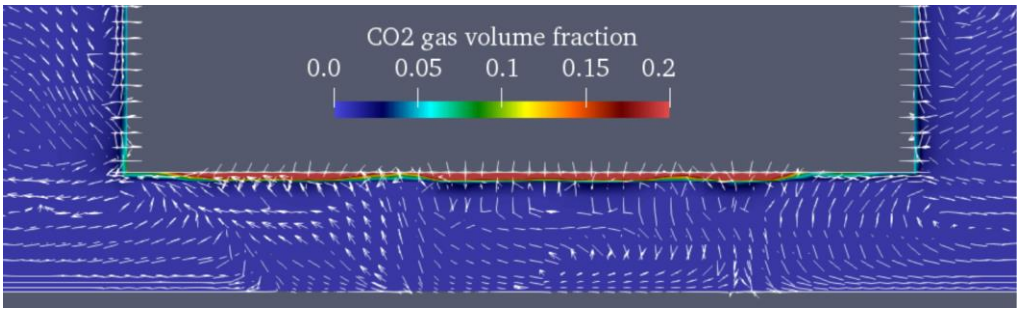

Figure 19. Flow patterns from bath-CO_2 interactions.

As seen in Figure 18 and Figure 20, the gas volume fraction is significantly higher at the bottom of the anode than the gas fraction on the anode sides.

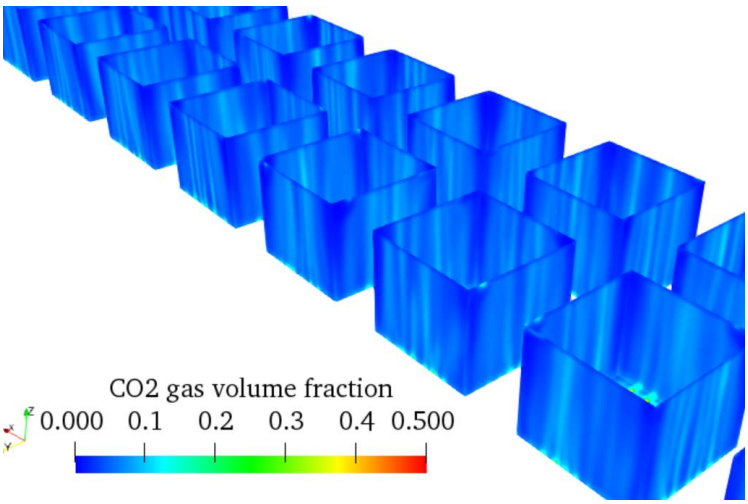

Figure 20. Instantaneous CO_2 bubbles rise from the sides of anodes.

This was caused by the high buoyancy force acting on the bubbles reaching the periphery of the bottom of the anode, which rose very quickly due to the large density difference (~2,050), thus resulting in minimal accumulation on the sides of the anodes. The buoyancy force acting in the bath-CO_2 system was approximately twice the buoyancy force observed for an air-water system, which only generates a density difference of approximately 1,000.

3.2.11 Turbulent Flow in the Bath

Investigation of flow inside a smelting cell is critical to understanding and optimizing the cell operation. The flow vortices inside the cell controlled the distribution of alumina. The anode effect (production of greenhouse gases) occurred at the locations of anode where the concentration of alumina was the lowest, and it propagated to other regions of the anode. The uniform distribution of alumina in the cell can prevent the anode effect. The flow structures that were generated in the cell were the primary driver of this uniformity. Moreover, cryolite will dissolve most potential wall materials: a layer of frozen cryolite must be formed on the vessel's walls to contain the bath, requiring a delicate heat balance in the cell partly controlled by the heat mixing caused by the vortices. Furthermore, the flow fluctuation induced by the CO_2 bubble motion underneath the anode can cause bath-metal interface fluctuations. This work, at this stage of development, ignored the MHD instabilities and MHD heave of the bath-metal interface.

Two mechanisms primarily drive the flow inside the bath:

a. CO_2 gas bubble rising to the top of the cell
b. The electromagnetic forces generated from the current passing through the cell.

The flow in the inter-anode space of the cell was primarily controlled by CO_2 gas bubbles, as shown in Figure 21. The rising plume of bubbles sheared the bath fluid to generate vortices that detached from the plume and appeared to meander in the inter-anode space, causing flow fluctuations until dissipation rendered to the smallest eddies, which may be resolved. The length scale of a typical vortex generated appears to be half the inter-anode distance.

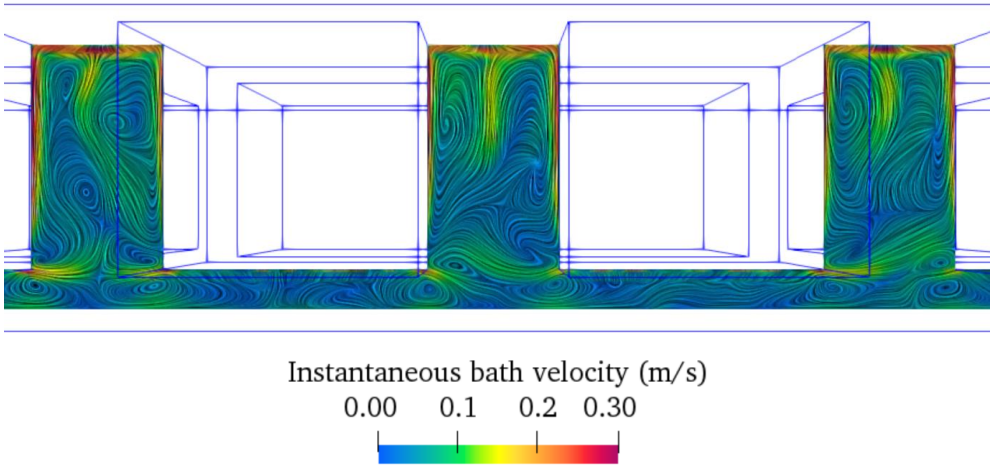

Figure 21. Inter-anode instantaneous profiles in the bath.

A pair of vortices was observed at the intersection of side and bottom anode surfaces. The length scale of the vortex seemed to be the same as the ACD length. It is evident from the average velocity profile in the vertical section plane (Figure 22) that two pairs of symmetric vortices were formed in the inter-anode space, and a pair of vortices was formed in the ACD space. The pair of vortices at the top of the inter-anode space is anisotropic, with a larger span width in the *z*-direction than the *x*-direction, spanning almost ¾ of the height of the anode. The corner pair of vortices appear to be less anisotropic than the top pair, and the corner pair has much smaller scales.

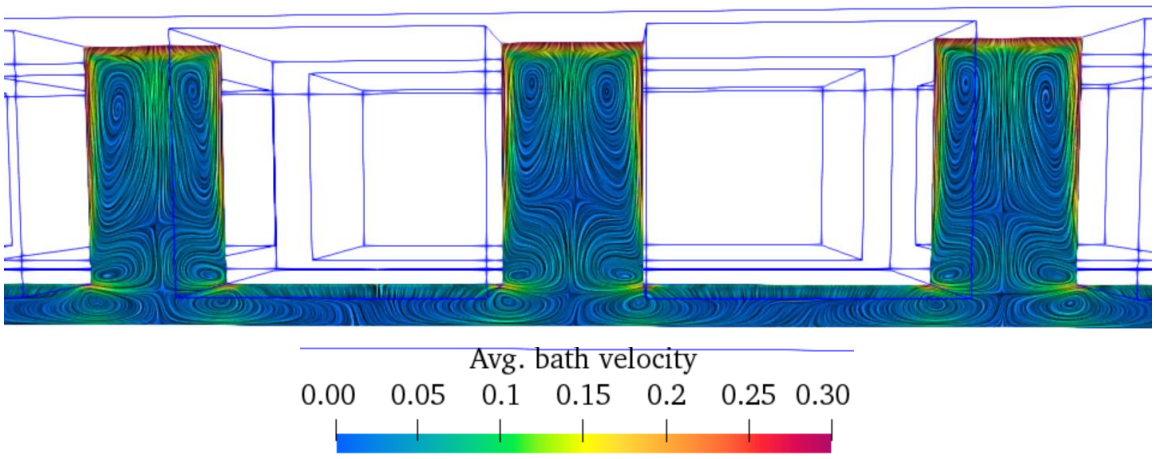

Figure 22. Inter-anode average bath velocity magnitude.

The second mechanism that controls flow in a smelting cell is the electromagnetic force, or the Lorentz force, generated from the interaction of the cell's current and magnetic field. Note that the magnetic field generated by the current passing through the bus bars and the ferromagnetic impact of the steel shell was neglected in the current study. These forces are mainly dominant in the ACD space as a result of the higher current density compared to the inter-anode regions. Therefore, the flow fluctuations generated from the Lorentz force were mainly constrained to the ACD space. There may have been flow interactions between the CO_2 and the Lorentz force–induced flows. The instantaneous bath velocity on a plane cutting the mid-ACD space is shown in Figure 23 (top). A plethora of vortices was generated in the ACD space because of the action of the Lorentz force on the fluid. The length scales of these vortices were significantly smaller than those in the inter-anode vortices. The smaller vortices are always more effective in mixing than the large vortices. Therefore, alumina entering this space will be quickly distributed to the anodes. The averaged velocity profiles (Figure 23, bottom) show the predominant vortices that controlled the flow in the ACD space. Four vortices can be seen in each outer corner of the anodes, along with two vortices in the inner corners whose axes are parallel to the *z*-direction or the height of the anodes. It appears that the vortices with axes parallel to the *x*-direction were generated at each edge of the anodes. In most studies, alumina is fed to the central channel. The vortices generated in the corners and edges of the anodes facing the central channel control the alumina distribution in the ACD space of the central channel. This outlines the potential of the relative importance of having alumina feeders between two anodes or between four anodes.

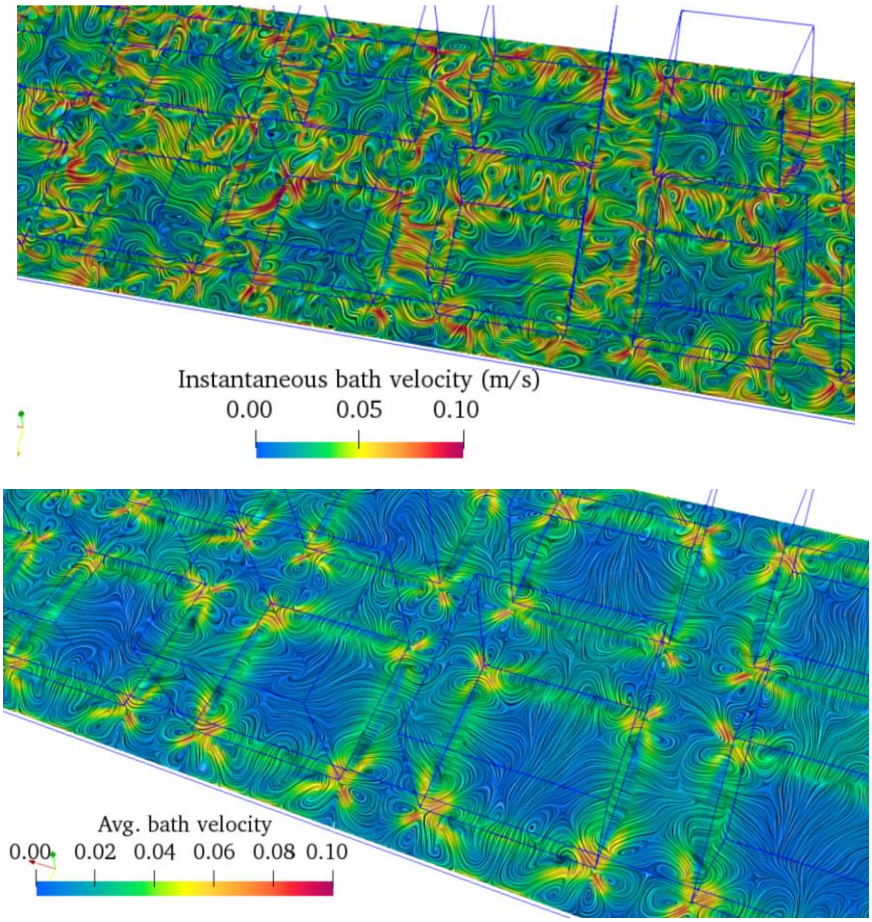

Figure 23. Instantaneous bath velocity (top) and averaged velocity (bottom) on a plane cutting mid-ACD space.

Turbulent kinetic energy (TKE) and normal Reynolds stress (RS) components on a plane cutting the anodes near the outlet are shown in Figure 24. TKE is higher away from the wall toward the center of the inter-anode gap. This behavior is expected in the inter-anode gap due to the interaction of the vortices generated from both sides of the anodes. The normal component of RS in the *z*-direction is higher than the normal components in the *x*- and *y*-directions in the inter-anode gap, which shows that the mixing is dominant in the *z*-direction. The normal component of RS in the *x*-direction is lower than in the *y*-direction in the inter-anode gap because of the higher dissipation of fluid fluctuations by the anode walls on either side of the inter-anode gap. However, in the central channel, the normal component of RS in the *y*-direction is lower than in the *x*-direction because of the resistance of the anode walls enclosing the central channel. The RS components in the side channel are insignificant compared to those in all other regions. This is expected because of the absence of the vortex interactions in the side channel compared to other regions.

TKE and normal RS components on plane 2 (below plane 1) are shown in Figure 25. The values of TKE and RS components are lower than the values observed for plane 1. The lower value of RS compared to plane 1 can be attributed to the negligible vortex interactions on this plane. The components of RS in plane 2 follow a trend similar to that of plane 1: that is, the component in the *z*-direction is higher than the components in *x*- and *y*-directions. Furthermore, the *x*-direction component is higher than that in the *y*-direction in the central channel and vice-versa in the inter-anode gaps.

TKE and RS components on the plane cutting the ACD space (plane 3) are shown in Figure 26. In the ACD space, the RS component in the *z*-direction is negligibly small compared to the *x*- and *y*-directions in all regions. In the inter-anode gap of the ACD space, the RS component in the *y*-direction is negligible compared to the *x*-direction and vice-versa in the central channel of the ACD space. This behavior of normal components of Reynolds stresses is understandable as ACD space is primarily dominated by horizontal velocities, and the importance of different horizontal velocity components is critical between two (x- and y-) inter-anode distances in the ACD region, as explained further. Upon inspecting a plane perpendicular to plane 3 (see Figure 27), it can be inferred that the higher value of RS_{xx} can be attributed to the interaction of two counter-rotating vortices whose axes are parallel to the *y*-axis. Similar vortex interactions can be found in the central channel of the ACD space; however, the vortex axis will be parallel to the *x*-axis, leading to a higher RS_{yy} component. The turbulence in the inter-anode gap and the central channel of ACD space behaves differently than the inter-anode spaces (planes 1 and 2) and the central channel (planes 1 and 2). The RS component in the *y*-direction is dominant compared to that in the *x*-direction and vice-versa in the central channel for planes 1 and 2. However, the RS component in the *x*-direction is dominant compared to the *y*-direction in the inter-anode gap of the ACD space and vice-versa for the central channel of the ACD space. Moreover, these RS components are more significant than those in plane 2 and are smaller than those in plane 1.

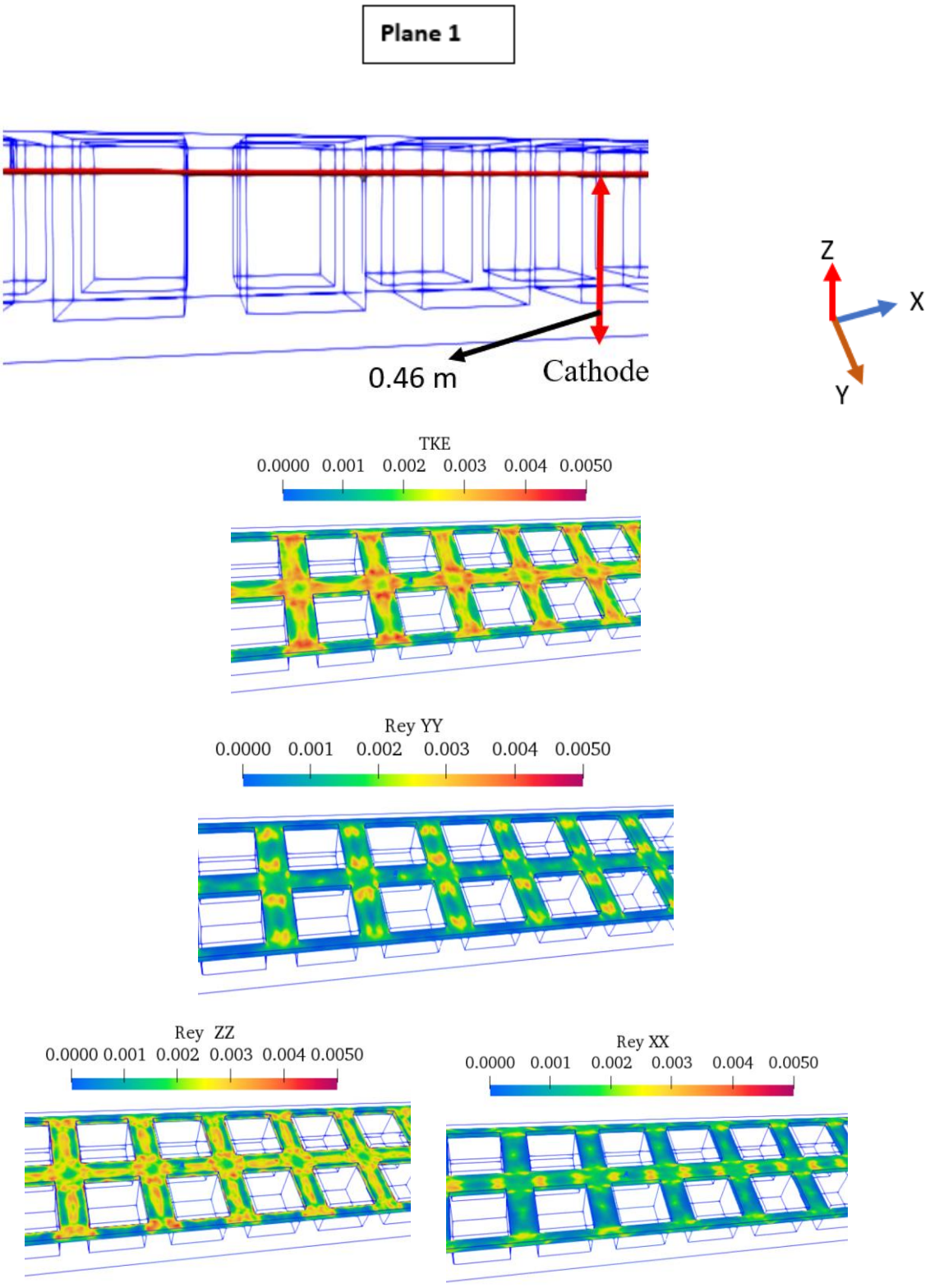

Figure 24. Components of TKE and RS on a horizontal plane near the outlet of the electrolytic cell.

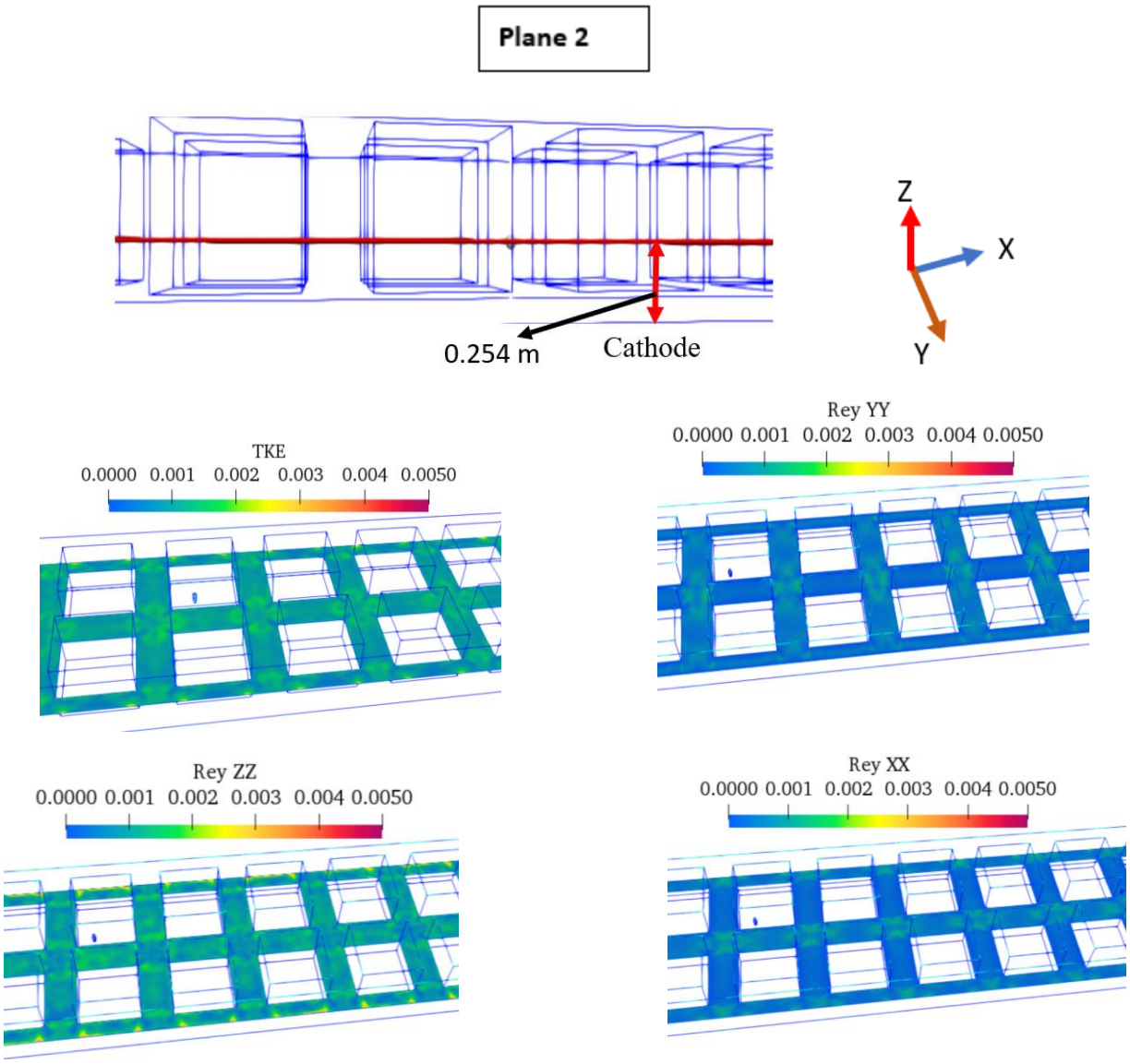

Figure 25. TKE (m2/s2) and RS (m2/s2) components on a plane cutting anodes below plane 1.

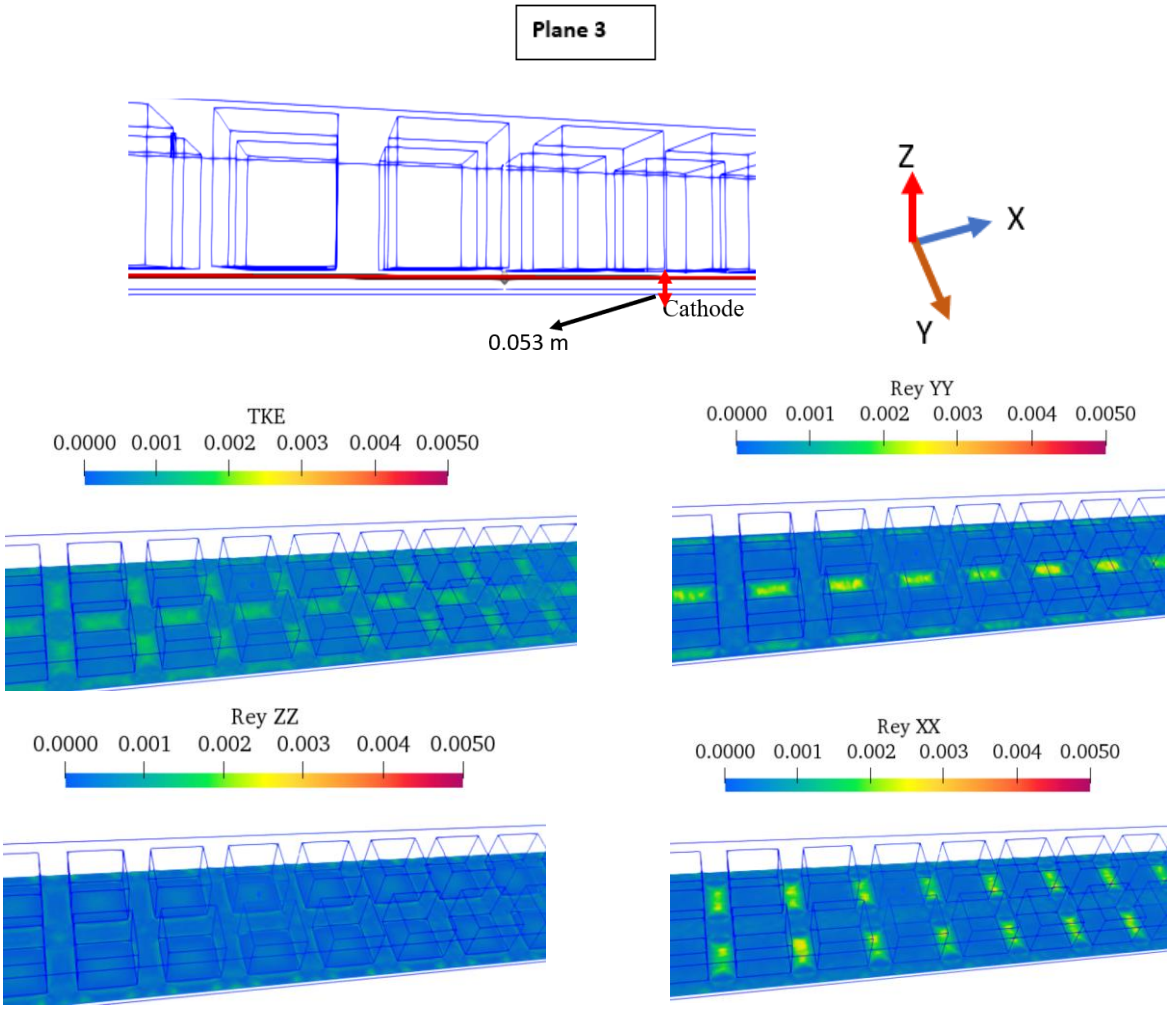

Figure 26. TKE (m2/s2) and RS (m2/s2) components on a plane cutting the ACD space.

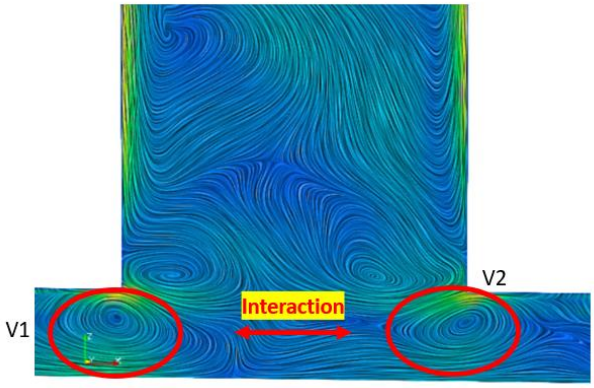

Figure 27. Vortices on a vertical plane cutting the ACD space.

3.2.12 Profiles from Linear Probes Across the Electrolytic Cell

Probes are placed at different cell regions to acquire the instantaneous velocity readings with time (see Figure 28). Probes9 and 11 are placed at the mid-point on either side of the anode. The velocity

fluctuation in the *z*-direction is higher than the fluctuations in the *x*- and *y*-directions for probes 9 and 11 (see Figure 29, bottom left and top right) because of the symmetry of the flow on both sides of the anode probes 9 and 11 show the same behavior.

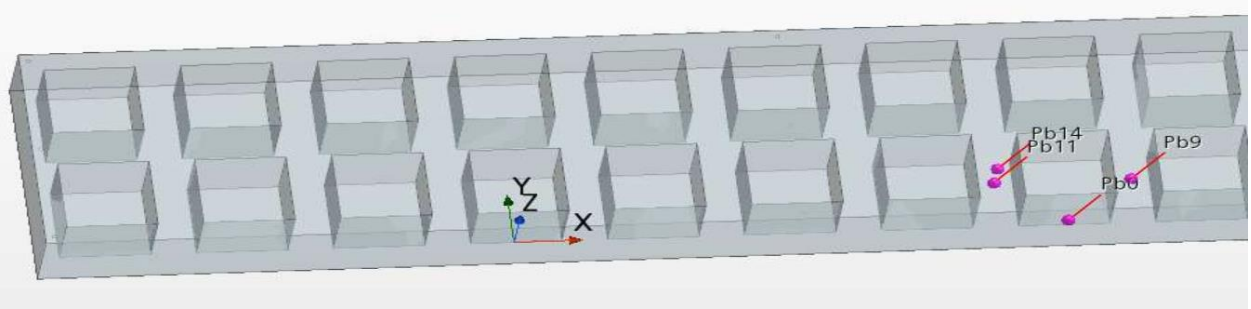

Probes in the inter-anode space.

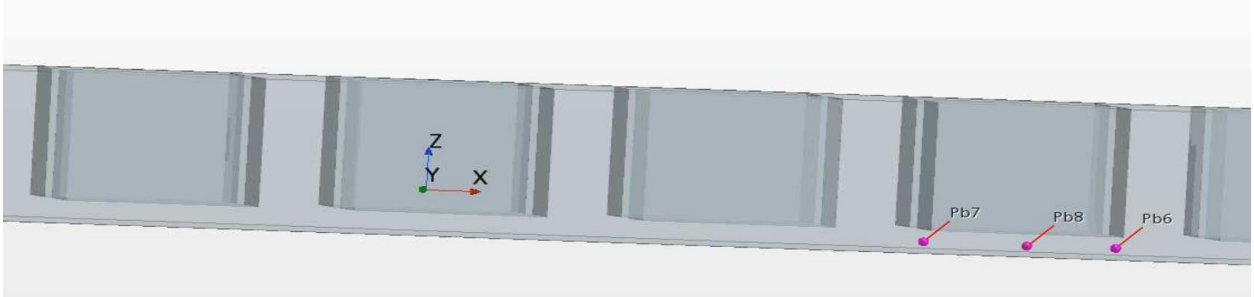

Probes in the ACD space.

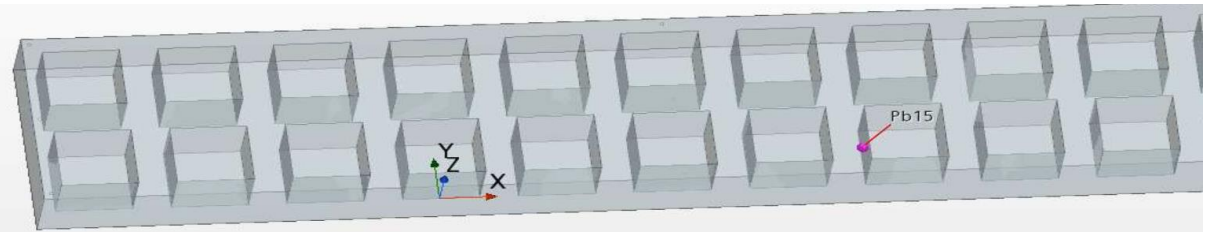

Probe on the left boundary of the anode.

Figure 28. Numbered probe locations in the cell.

The velocity fluctuations for probe 0 (see Figure 29 top left) in the *z*-direction are significantly lower than those for probes 9 and 11 due to the absence of counter-rotating vortex interaction. It can also be observed that the fluctuations in the other directions are small compared to those in the components of probes 9 and 11. This may be due to the higher resistance to fluctuations in the smaller gap between the anode and sidewall compared to the more significant gap between two anodes. Probe 14 (see Figure 29, top right) was placed below the bath-air/gas interface. The fluctuations observed for probe 14 are significantly higher than those of probes 9, 11, and 0 in all directions, particularly in the z-direction. It appears that the vortices generated by the bubble plumes of either side interacted strongly at this point, causing fluctuations far superior to the turbulent fluctuations detected by other probes in the inter-anode gaps. This highlights the turbulent nature of the bath-air interface. In a real cell, the bath-air interface is generally covered with a crust, and therefore this behavior may be a bit dampened and expected slightly lower location in the bath below bath crust-liquid bath interface.

Probes 6 and 7 were placed underneath the anode bottom edges in the ACD space. The velocity fluctuation in the *x*-direction was predominant (see Figure 30) over the fluctuations in the other directions.

The presence of the anode bottom wall dampened the fluctuation in the *z*-direction, and the vortex whose axis was in the *y*-direction underneath the anode edge caused significant fluctuation in the *x*-direction compared to that in the *y*-direction. The predominant *x*-direction fluctuation was negative for probe 6 and positive for probe 7 because of the counter-rotating vortices underneath those locations. Probe 8 showed higher fluctuation in the *y*-direction than in the *x*- and *z*-directions. This was as expected as a result of the vortex formed in this location, whose axis is parallel to the *x*-direction. Probe 15, placed near the boundary where bubbles were rising, showed a higher fluctuation in the *z*-direction (see Figure 31) and negligible fluctuations in the other directions. The buoyant rise of bubbles in the z-direction caused the fluctuation to dominate in the *z*-direction. The damping from the bubbles in the *y*-direction and the anode sidewall in the *x*-direction dissipated the fluctuation in the *y*- and *x*-directions.

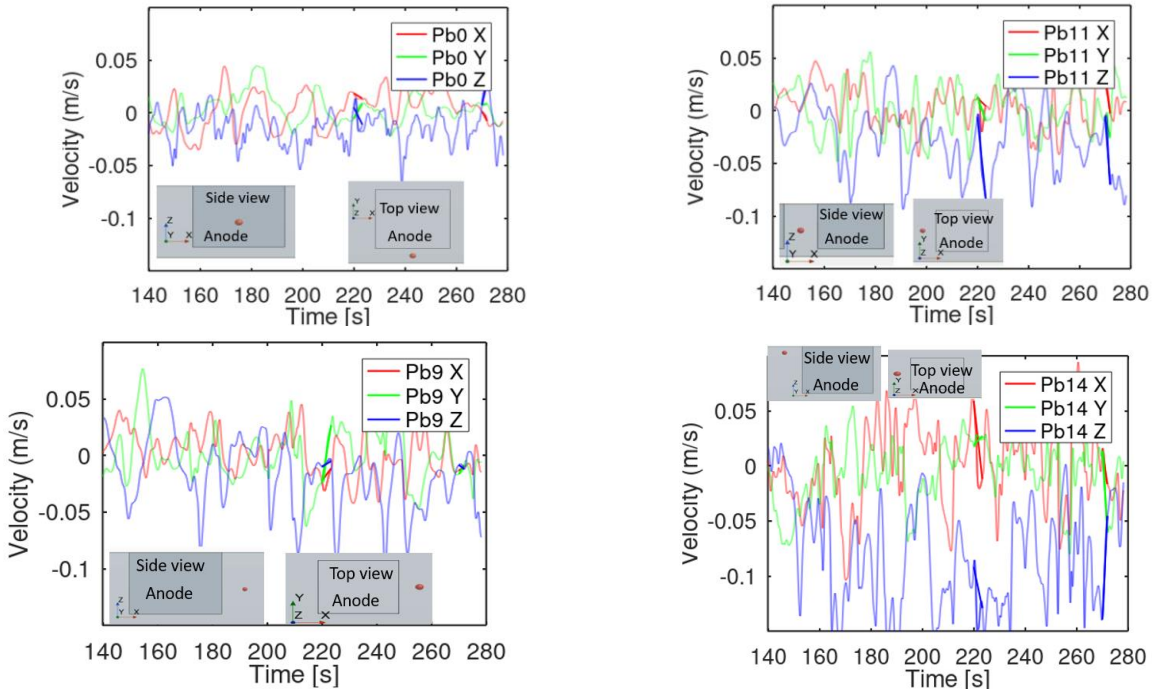

Figure 29. Probes inter-anode spaces: probes 0 (top left), 11 (top right), 9 (bottom left), and 14 (bottom right).

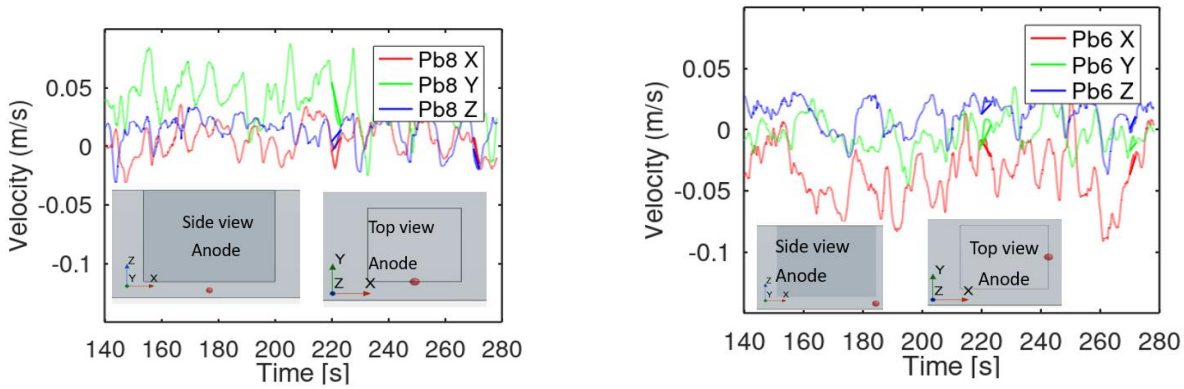

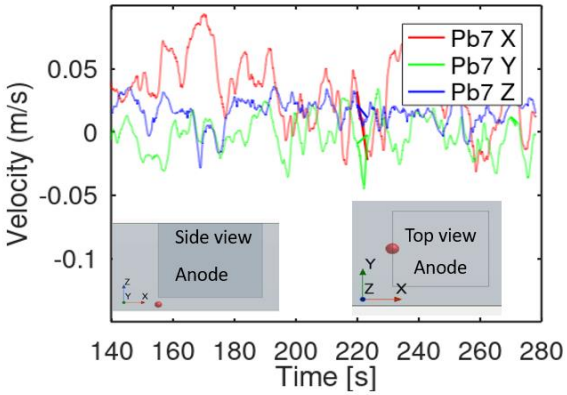

Figure 30. Probes in the ACD space at anode bottom edge.

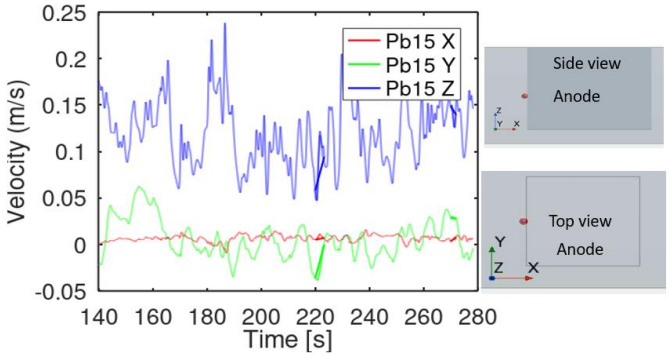

Figure 31. Probe boundary at the bath-air interface in the inter-anode gap.

3.2.13 Turbulent Kinetic Energy Spectra

TKE distribution with frequencies in different regions of the cell is shown in Figure 32. The most dominant frequencies that contain the majority of the TKE were in the range of 1–100 Hz, and the spectra were nearly the same for all the regions. The TKE distributed in the inertial range followed the universal law of the -5/3. The dissipation near the top wall region was slightly higher than in other regions, which was expected due to the free-slip boundary restriction flow in the vertical direction.

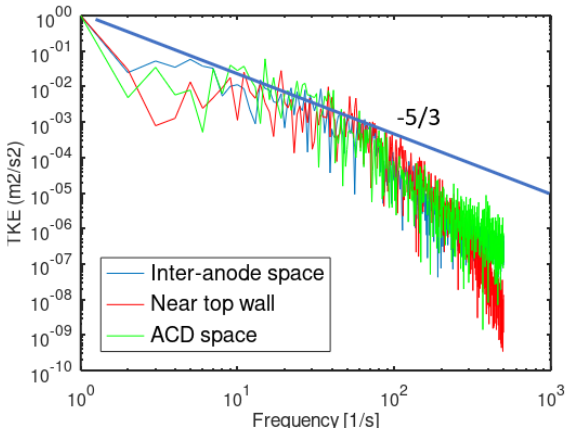

Figure 32. TKE spectrum at critical regions of the *electrolytic* cell.

3.2.14 Dissolution and Transport of Alumina

It is crucial to accurately predict alumina distribution inside the cell in powder and dissolved bath phases. The dissolved alumina concentration controls the anode effect and causes voltage oscillations. The distribution of alumina in the powder phase controls sludge formation (mucking effect) and bath temperature variations caused by specific heat and heat of dissolution. Previous studies (Feng, et al., 2011) (Zhang, et al., 2014) (Eick, et al., 2015) did not model the powder phase of alumina; instead, an instantaneous dissolution of alumina powder was assumed upon injection. In the present study, alumina powder was modeled as a solid phase, but the size change of the powder particles from dissolution was not considered.

Solid alumina powder of mean uniform size (100 microns) was fed through all four feeders to match the net consumption rate of alumina on the anodes, which is 0.0304 kg/s for a current of 175kA. The solids that entered the bath got dissolved to form liquid alumina. This liquid alumina was dispersed in the cell by the agitation from the CO_2 bubbles in the upper regions of the cell and the electromagnetic forces in the ACD space of the cell, without the need for a mechanical agitator. Figure 33 shows the mixing and transport of dissolved alumina from the 3D vortices generated by the bubbles and electromagnetic forces. It was observed that the vortices produced on the edges of each anode bottom drive the alumina (red globules) toward the center of the anode. The presence of these corner vortices was highly favorable for uniquely transferring the dissolved alumina to the bottom of the anode for an electrochemical reaction, thereby preventing a shortage of alumina.

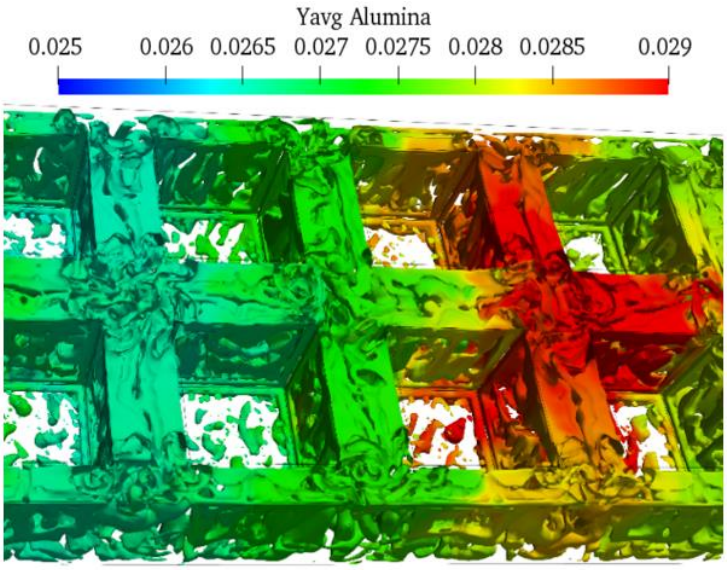

Figure 33. 3D circulation vortices of alumina in the electrolytic cell.

Likewise, the enhanced agitation from the vortex interactions in the inter-anode gap caused the alumina to be pulled from the central channel toward the inter-anode gap and side channels, resulting in mixing in the transverse direction of the cell. A similar conclusion can be derived for mixing in the central channel in the longitudinal direction of the cell. Figure 34 shows the instantaneous and average dissolved alumina mass fraction in the ACD space, which is primarily controlled by MHD and horizontal velocity due to the anode side releasing gas bubbles. The transmission of alumina in both the longitudinal and transverse cell directions is nearly the same.

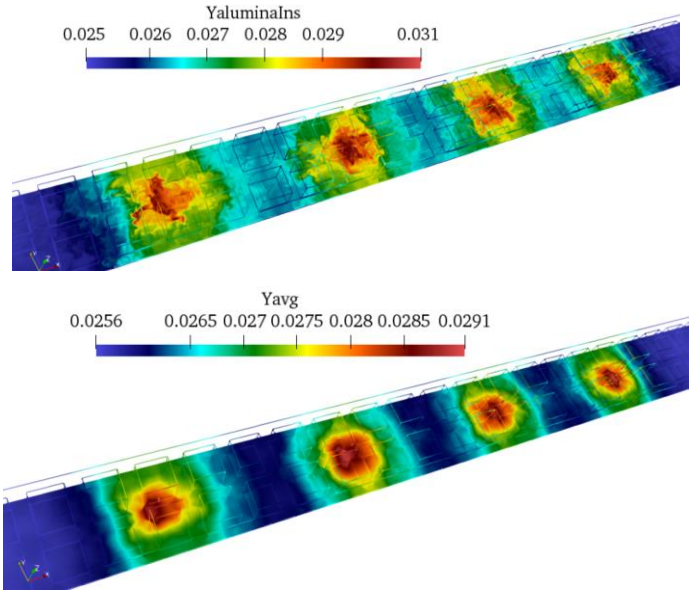

Figure 34. Instantaneous profiles on a horizontal plane through the mid-ACD space at t = 600 s, showing the mass fraction of dissolved alumina (top) and the average mass fraction of alumina (bottom).

The alumina solids that were fed through the feeder were primarily dissolved in the bath before settling to the cathode. However, a small concentration of undissolved solids reached the ACD space and was dispersed by the vortices, as shown in the horizontal plane of Figure 35. Red spots of dissolved alumina mass fraction can be seen in those spots where the solids enter, like the spots on the vertical plane in Figure 35 underneath the bottom of the anode. This amount of undissolved alumina may be lower if real alumina particle size distribution is considered, which provides a higher specific area for dissolution. The dissolved alumina fraction on all of the anodes after 10 minutes of cell operation is presented in Figure 36.

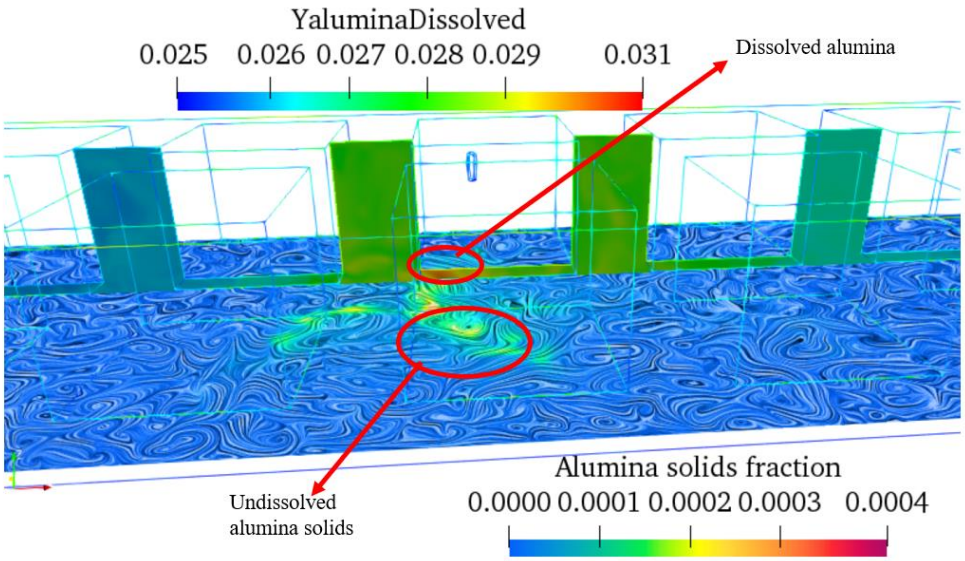

Figure 35. Settling and dispersion of solid alumina from vortices produced by electromagnetic force: horizontal plane shows solids, and vertical plane shows dissolved alumina.

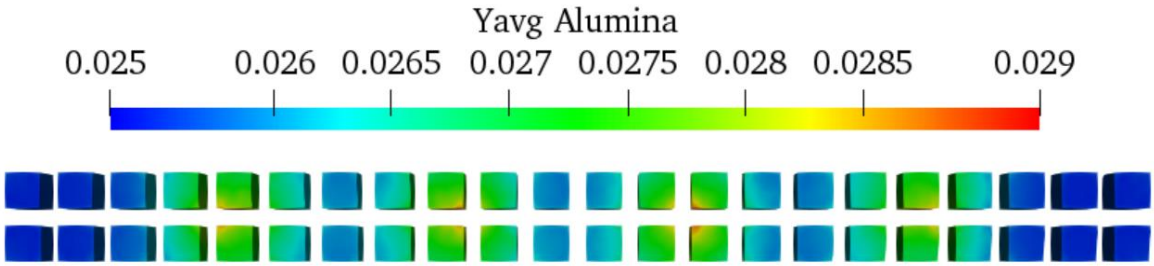

Figure 36. Time-averaged mass fraction of dissolved alumina at t = 600 s.

The mass fraction of alumina on the anodes at the left and right corners seems to be significantly lower (≤ 2.5 %) compared to the fraction of alumina on the anodes in the other regions. Therefore, these anodes tend to show the anode effect. To confirm a true anode effect, the anodic diffusion layer should be sufficiently resolved, and calculations must be performed long enough to achieve a stationary state in the cell operation. This work, at this stage of development, never intended to confirm the anode effect; rather, the focus remained only on predicting the vulnerability of different location anodes to anode effect and showcase model capabilities.

3.2.15 Bath Temperature Distribution

The temperature of the liquid bath in aluminum smelting must be maintained at an operating temperature of around 960oC. Large thermal variations in the bath lead to unstable cell operation. It is imperative to maintain electrolytic bath temperature by passing enough current through the smelting cell. The electrical energy needs to be supplied to offset the heat losses from the cell to the atmosphere, heating the solid cold alumina to operating temperature, providing the heat of dissolution for alumina and enough voltage for aluminum production. This work primarily focused on the alumina side of the operation of the cell, and therefore, at this stage of development, only the sensible bath heat loss and heat of dissolution are incorporated in the model. Heat-balance aspects of the self-heated cell design are not considered in the modeling work.

The regions in a cell that are susceptible to cooling from dissolution are indicated in Figure 38. The cold spot's formation in the feeder's vicinity is evident from the maximum dissolution in that region. A small patch of cold spots can be observed in the inter-anode space. The correlation of the solid fraction and the bath temperature drop is expected, as shown in Figure 37. The average bath temperature (Figure 38) indicates cold spots that are symmetric near the feeder, gradually vanishing in the inter-anode space. Figure 38 shows that the undissolved solids reach the anode bottoms and produce patches of cold spots while dissolving in those regions.

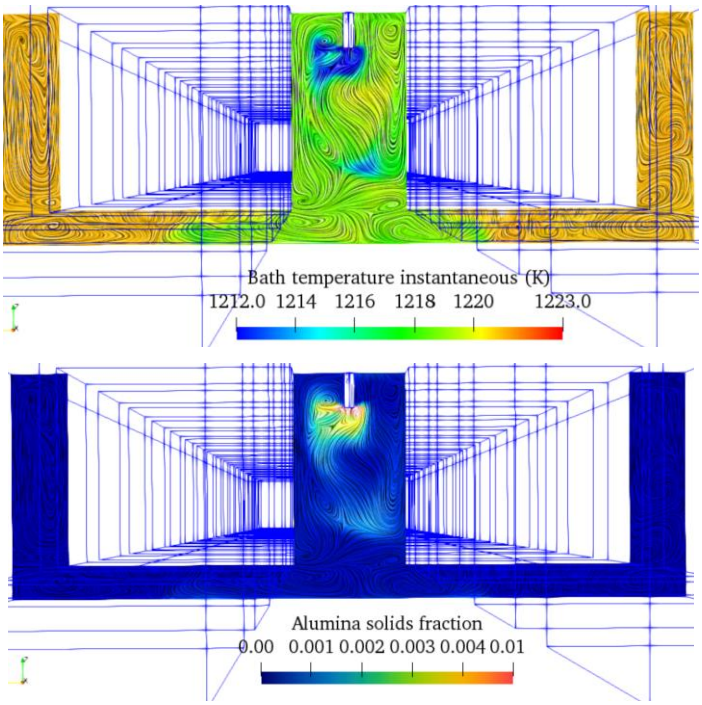

Figure 37. Instantaneous bath temperature and alumina solids fraction after 10 min of operation.

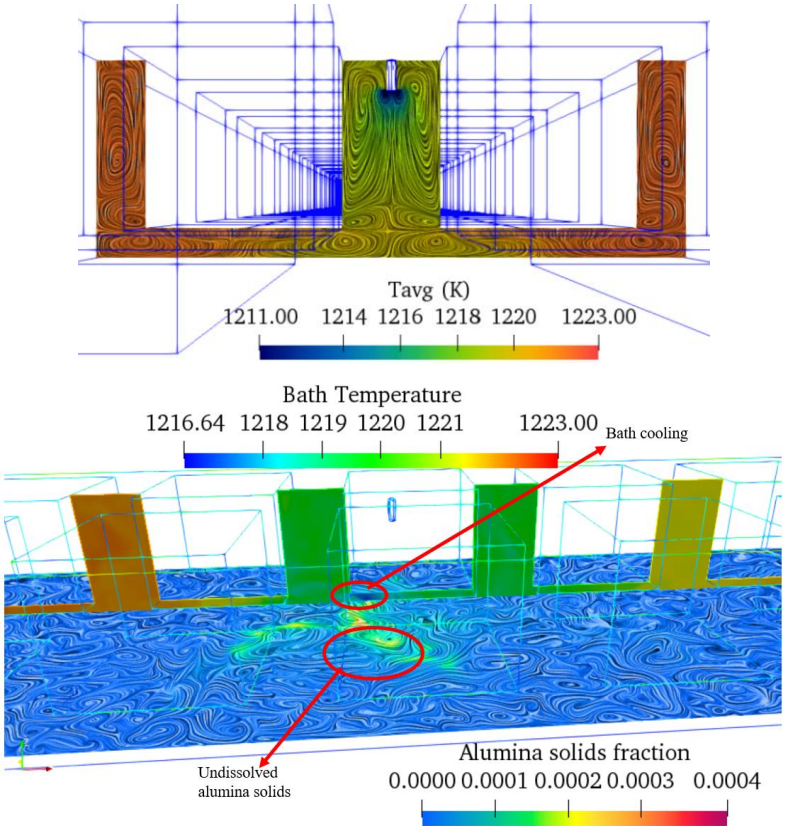

Figure 38. Average bath temperature and instantaneous solids fraction of alumina in the ACD at t = 600 s.

4. COMMERCIALIZATION POSSIBILITIES

None.

5. PLANS FOR FUTURE COLLABORATION

Throughout this project, several areas of potential collaboration and future research were identified, as follows:

- Device-scale modeling using first-principles, high-fidelity physics on HPC systems
  - Evaluate new operating conditions, or process parameters, to reduce the device's carbon footprint,
  - Carbon-conscious process optimization,
  - Computational screening for various carbon-reduction measures,
  - Reduce technical risks of deploying innovative retrofittable technologies,
  - Accelerate technology maturation or readiness levels,
  - Understand prototype scale up for a real system.

We will continue to look for any new collaboration opportunities that are supported through various program offices in the US Department of Energy.

6. CONCLUSIONS

Alcoa and ORNL have collaborated under a Cooperative Research and Development agreement to develop an open-source simulation tool that can predict the aluminum smelting process in an innovative energy-efficient smelting cell developed by Alcoa. This tool can also be used for the design and development of smelters. This report discusses the details of the CFD model and code modification performed in OpenFOAM to develop the tool for smelting. This report also investigates how the turbulent coupled multiphysics performed on a conventional smelter using the tool can further advance conventional smelting design concepts.

Low-fidelity RANS models are predominantly used to conduct smelting simulations to aid in the design process; however, RANS cannot predict the highly transient turbulent vortical structures of the flow coupled multiphysics involved in a smelting process. The tool developed in this work can be used to perform high-fidelity LES of smelting to provide valuable insights on the smelting turbulence. This capability can be applied to help solve the common design challenges in smelter development: identifying the location of the aluminum feeder for maximum productivity and reduced emissions, identifying, and mitigating bath cold spots caused by the dissolution of alumina, and mitigating CO_2 gas accumulation on the anode bottom and associated high voltage consumption. Below are the significant findings from the LES study conducted on a conventional smelter cell with 22×2 anodes and 175kA passing through the cell:

1. The CO_2 gas fraction pattern at the anode bottom shows peaks and valleys similar to the bubble nucleation observed in boiling applications. The gas volume fraction at the periphery of the anode bottom is significantly lower than it was toward the center. It appears that the bubble-induced bath vortex that forms at the periphery of each anode drives the gas bubbles at the periphery toward the sides, resulting in a lower gas accumulation. Thus, bath flow vortices formed in the cell partially reduce the current resistance caused by high CO_2 gas accumulation.

2. Flow in the cell's inter-anode space is primarily controlled by buoyant CO_2 gas bubbles, not by Lorentz forces from the negligible current density in the inter-anode space. The rising plume of bubbles shears the bath fluid to generate turbulent vortical structures, causing flow fluctuations in this region. The length scale of a typical vortex generated appears to be half the inter-anode distance. The averaged flow field shows a pair of symmetric, anisotropic vortices in the inter-anode with a larger span width in the *z*-direction than in the *x*-direction. The averaged flow field spans almost ¾ of the height of the anodes. The averaged flow field in the inter-anode gaps also shows a pair of vortices generated at the bottom edge of the side anode surfaces. The regions of the averaged flow field on the vertical plane in the ACD space show vortices on the edges of the anode bottom surfaces whose length scales are proportional to the ACD length. The length scales of the vortices in the inter-anode gaps appear much more significant than those in the ACD space. Unlike the inter-anode gap, the turbulence generated in the ACD space is most likely caused by the interaction of bubble and Lorentz forces.

3. Normal Reynolds stresses are higher in the upper region of the inter-anode gap than in the lower region. The component in the *z*-direction dominates over the components in the *x*- and *y*-directions. However, in the ACD space, the *x*- and *y*- direction components dominate the *z*-direction. The Reynolds stresses induced by the bubbles in the inter-anode gap are higher than in the ACD space. The difference in the behavior of Reynolds stresses in the inter-anode gap, and the ACD space can be attributed to the difference in vortex interactions occurring in both regions. The interactions of the pair of vortices generated on the side surfaces of the anodes are causing the Reynolds stresses to be higher in the upper region of the inter-anode gap. However, the

Reynolds stresses in the ACD space are controlled by the interaction of a different pair of vortices generated at the edges of anode bottom surfaces.

4. The TKE distribution at different critical regions of the cell shows that the most dominant frequencies containing a significant portion of the TKE are in the range of 1–100 Hz. The TKE distribution in the inertial range follows the universal -5/3 law. The dissipation near the top wall region is high as a result of the free-slip boundary damping. Hence, the TKE spectrum shows a steep descent at high frequencies compared to spectra in other regions.

5. Alumina solids that are fed through the feeder are primarily dissolved in the bath before they settle to the cathode because of the small particle size chosen for the study. However, a small concentration of undissolved solids driven by the flow reaches the ACD space. Peaks in the dissolved alumina mass fraction are observed in the ACD space as a result of the entrance of these undissolved solids. This mucking behavior may be an overestimation of the assumption of single mean particle size in the dissolution model. In reality, with a range of particles sizes involved, alumina available for dissolution will have a much larger specific area. Formation of the vortices at the edge of the anode's bottom surface is highly favorable for uniquely transferring the dissolved alumina to the anode bottom surfaces for electrochemical reaction. The transmission of alumina caused by the flow in both longitudinal and transverse cell directions is nearly the same, showing no preferential direction bias for the cell design. After 10 min of operation, the dissolved alumina fraction on the six anodes toward the left and right ends of the cell seems to be significantly lower ($\leq$ 2.5 %). Therefore, these anodes are prone to anode effect in the existing feeder setup. The resolution of the anodic diffusion layer and stationary results are needed to ascertain the true possibility of the anode effect.

6. Cold spots near the feeders were observed as a result of the higher dissolution of alumina. The average bath temperature indicates that cold spots were symmetric near the feeders, and they gradually vanished in the inter-anode space. The undissolved solids were driven by the flow toward the anode bottoms, and they produce patches of cold spots while dissolving in those regions.

7. REFERENCES

Alam M. [et al.] Investigation of electrolytic bubble behavior in aluminum smelting cell [Journal] // Light Metals. - 2003. - pp. 591-596.

Baiteche M. [et al.] LES turbulence modeling approach for molten aluminum and electrolyte flow in aluminum electrolysis cell [Journal] // Light Metals. - 2017. - pp. 679-686.

Cubeddu A., Nandana V. and Janoske U. A numerical study of gas production and bubble dynamics in a Hall-Heroult reduction cell [Journal] // Light Metals. - 2019. - pp. 605-613.

Das S., Brooks G. and Morsi Y. Theoretical investigation of the inclined sidewall design on magnetohydrodynamic (MHD) forces in an aluminum electrolytic cell [Journal] // Metallurgical and Materials Transactions B. - 2011. - Vol. 42. - pp. 243-253.

Dhotre M. T. [et al.] Large-eddy simulation for dispersed bubbly flows: a review [Journal] // International Journal of Chemical Engineering. - 2013.

Drew Donald A. and Passman Stephen L. Theory of multicomponent fluids [Journal] // Springer Science and Business Media. - 2006. - Vol. 135.

Eick I. [et al.] Coupled multiscale multiphysics simulation framework for aluminum electrolysis [Conference] // In Eleventh International Conference on Computational Fluid Dynamics in the Minerals and Process Industries. - 2015.

Einarsrud K. E. [et al.] Towards a coupled multiscale, multiphysics simulation framework for aluminum electrolysis [Journal] // Applied Mathematical Modeling. - 2017. - Vol. 44. - pp. 3-24.

Feng Y. Q. [et al.] CFD model of bubble driven flow in aluminum reduction cells and validation using PIV measurement [Conference] // In Fifth International Conference on Computational Fluid Dynamics in the Process Industries. - 2006.

Feng Y., Cooksey M. A. and Schwarz M. P. CFD modeling of alumina mixing in aluminum reduction cells [Journal] // Light Metals. - 2011. - pp. 543-548.

Fox R. O. On multiphase turbulence models for collisional fluid-particle flows [Journal] // Journal of Fluid Mechanics. - 2014. - Vol. 742. - pp. 368 - 424.

Fox Rodney O. Large-eddy-simulation tools for multiphase flows [Journal] // Annual Review of Fluid Mechanics. - 2012. - Vol. 44. - pp. 47-76.

Frossling N. Uber die verdunstung fallernder tropfen [Journal] // Gerlands Beitr. Geophys.. - 1938. - Vol. 52. - pp. 170-216.

Gerbeau J. F., Lelievre T. and Le Bris C. Simulations of MHD flows with moving interfaces [Journal] // Journal of Computational Physics. - 2003. - Vol. 184. - pp. 163 - 191.

Hua J. [et al.] Numerical simulation of multiphase magnetohydrodynamic flow and deformation of electrolyte-metal interface in aluminum electrolysis cells [Journal] // Metallurgical and Materials Transaction B. - 2018. - Vol. 49. - pp. 1246-1266.

Li J. [et al.] An inhomogeneous three-phase model for the flow in aluminium reduction cells [Journal] // International Journal of Multiphase Flow. - 2011. - Vol. 37. - pp. 46-54.

Liu X. [et al.] CFD modeling of alumina diffusion and distribution in aluminum smelting cells [Journal] // JOM. - 2019. - Vol. 71. - pp. 764-771.

Mankad S., Nixon K. M. and Fryer P. J. Measurements of particle-liquid heat transfer in systems of varied solids fraction [Journal] // Journal of food engineering. - 1997. - 1: Vol. 31. - pp. 9 - 33.

Munger D. and Vincent A. A level set approach to simulate magnetohydrodynamic instabilities in aluminum reduction cells [Journal] // Journal of Computational Physics. - 2006. - Vol. 217. - pp. 295-311.

Naumann Z. and Schiller L. A drag coefficient correlation. [Journal] // Z. Ver. Deutsch. Ing. - 1935. - 318: Vol. 77. - p. e323.

Panicker N. S. [et al.] COMPUTATIONAL MODELING AND SIMULATION OF ALUMINIUM SMELTING PROCESS USING OpenFOAM [Conference] // 5-6th Thermal and Fluids Engineering Conference. - Chicago : [s.n.], 2021.

Panicker N., Passalacqua A. and Fox R. O. Computational study of buoyancy-driven turbulence in statistically homogeneous bubbly flows [Journal] // Chemical Engineering Science. - 2020. - Vol. 216. - p. 115546.

Panicker N., Passalacqua A., and Fox R. O. On the hyperbolicity of the two-fluid model for gas-liquid bubbly flows [Journal] // Applied Mathematical Modeling. - 2018. - Vol. 57. - pp. 432 - 447.

Portuousi M., Sahu J. N. and Ganesan P. Effect of interfacial forces and turbulence models on predicting flow pattern inside the bubble column [Journal] // Chemical Engineering and Processing: Process Intensification. - 2014. - Vol. 75. - pp. 38 - 47.

Ranz W. E. Evaporation form drops [Journal] // Chem. Eng. Prog. - 1952. - Vol. 48. - pp. 141 - 146.

Severo D. S. [et al.] Modeling magnetohydrodynamics of aluminum electrolysis cells with ANSYS and CFX [Journal] // Light Metals. - 2005. - pp. 475 - 480.

Skybakmoen E., Solheim A. and Sterten A. Alumina solubility in molten salt systems of interest for aluminum electrolysis and related phase diagram data [Journal] // Metallurgical and materials transactions B. - 1997. - 1: Vol. 28. - pp. 81 - 86.

Smagorinsky Joseph General circulation experiments with the primitive equations: I. The basic experiment [Journal] // Monthly weather review. - 1963. - pp. 99-164.

Song Y. [et al.] The impact of cathode material and shape on current density in an aluminum electrolysis cell [Journal] // JOM. - 2016. - Vol. 68. - pp. 593-599.

Spalding D.B. A single formula for the “law of the wall" [Journal] // Transactions of the ASME, Series E: Journal of Applied Mechanics. - 1961. - Vol. 28. - pp. 455 - 458.

Sun M. [et al.] Single and Multiscale Bubble Motions Beneath an Inclined Downward-Facing Surface in the Aluminum Reduction Cell [Journal] // Industrial & Engineering Chemistry Research. - 2020. - 17 : Vol. 59. - pp. 8403-8415.

Thonstad J. [et al.] The dissolution of alumina in cryolite melts [Journal] // Essential readings in Light Metals. - 2016. - pp. 105 - 111.

Wang Q. [et al.] Simulation of magnetohydrodynamic multiphase flow phenomena and interface fluctuation in aluminum electrolytic cell with innovative cathode [Journal] // Metallurgical and Materials Transactions B. - 2014. - Vol. 45. - pp. 272-294.

Welle H. G. [et al.] A tensorial approach to computational continuum mechanics using object-oriented techniques [Journal]. - 1998. - 6: Vol. 12. - pp. 620 - 631.

Zhan S. [et al.] Analysis and modeling of alumina dissolution based on heat and mass transfer [Journal] // Transactions of nonferrous metals society of China. - 2015. - Vol. 25. - pp. 1648 - 1656.

Zhan S. [et al.] CFD simulation of dissolution process of alumina in an aluminum reduction cell with two-particle phase population balance model [Journal] // Applied Thermal Engineering. - 2014. - Vol. 73. - pp. 805-818.

Zhang H. [et al.] Numerical simulation of alumina-mixing process with a multicomponent flow model coupled with electromagnetic forces in aluminum reduction cells [Journal] // Jom. - 2014. - Vol. 66. - pp. 1210-1217.

Zhang K. [et al.] Computational fluid dynamics (CFD) modeling of bubble dynamics in the aluminum smelting process [Journal] // Industrial & Engineering Chemistry Research. - 2013. - 33: Vol. 52. - pp. 11378-11390.

Zhang K. [et al.] Computational fluid dynamics (CFD) modeling of bubble dynamics in the aluminum smelting process [Journal] // Industrial & Engineering Chemistry Research. - 2013. - Vol. 52. - pp. 11378-11390.

Zhao Z. [et al.] Numerical Modeling of Flow Dynamics in The Aluminum Smelting Process: Comparison Between Air–Water and CO 2–Cryolite Systems [Journal] // Metallurgical and Materials Transactions B. - 2017. - 2: Vol. 48. - pp. 1200 - 1216.

Zikanov O. [et al.] A new approach to numerical simulation of melt flows and interface instability in Hall-Heroult cells [Journal] // Metallurgical and Materials Transactions. - 2000. - Vol. 31. - pp. 1541-1550.

APPENDIX A. CODE FLOW CHART

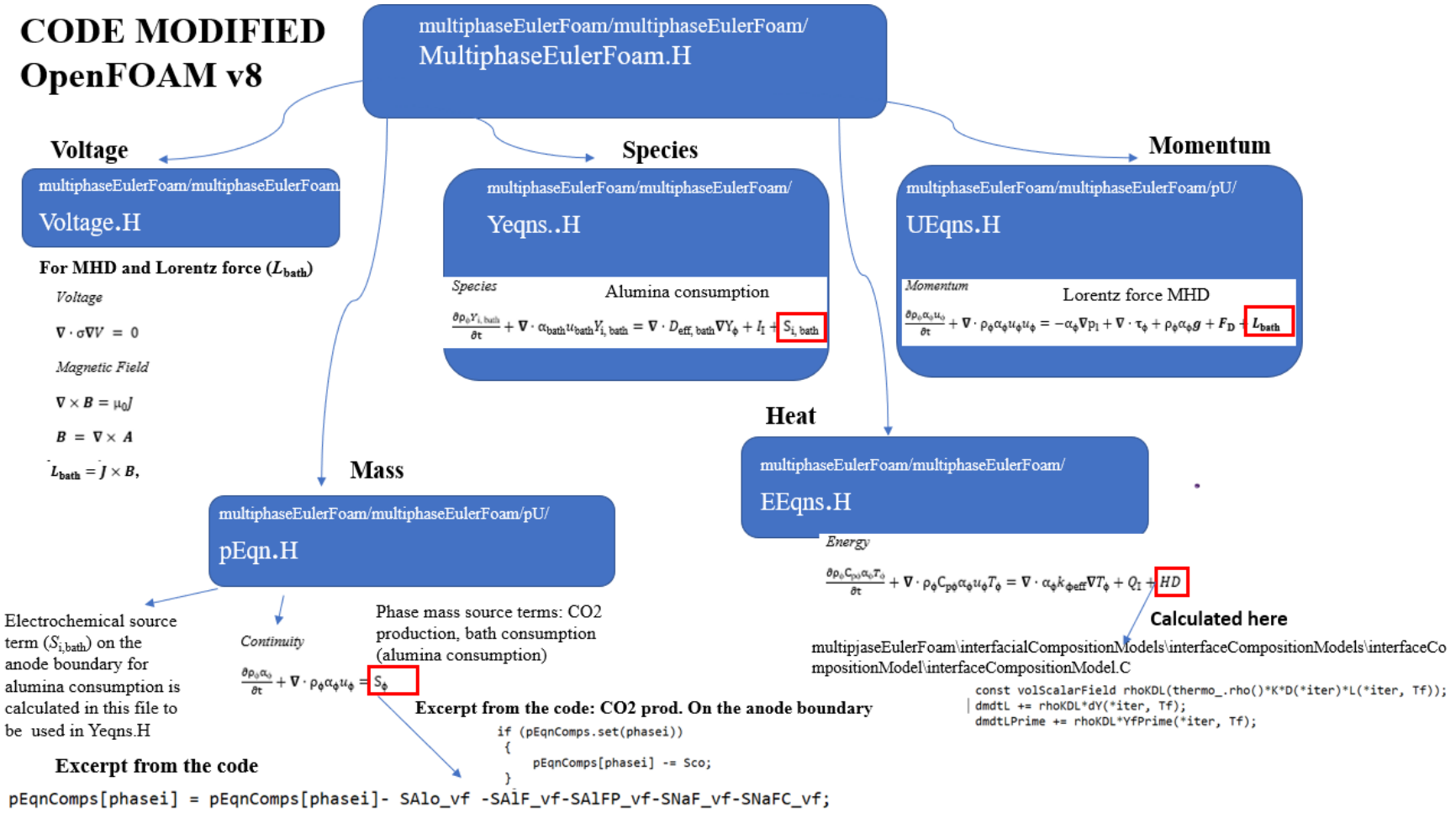

APPENDIX B. INPUT FILES

OpenFOAM Input files For LES Study

FOLDER to specify BCs and ICs

Bath = cryolite species + alumina species
Powder = alumina species

0

Files

- **A** - Magnetic vector potential
- **aldio.liquid** - Mass fraction of alumina in bath (Y_{al})
- **aldio.paldio** - Mass fraction of alumina in powder
- **alpha.liquid** - Volume fraction of bath
- **alpha.paldio** - Volume fraction of powder
- **alpha.particle** - Volume fraction of CO_2 gas
- **alphaT** - Turbulent thermal diffusivity
- **Cryoltie.liquid** - Mass fraction of cryolite in bath
- **SAlo** - Sink term for alumina in the bath
- **Sco** - Source term for CO_2 production
- **p** - Bath total pressure
- **P_rgh** - Bath dynamic pressure
- **nut** - Sub-grid bath viscosity
- **V**- Voltage
- **U.Paldio** - Velocity of powder
- **U.particle** - Velocity of CO_2 gas
- **U.Liquid** - Velocity of bath
- **T.liquid** - Temperature of bath
- **T.Paldio** - Temperature of bath
- **T.Particle** - Temperature of gas
- **Rey_s** – Reynolds stress bath
- **Utot** – Intermediate avg. velocity
- **Ytot** – Intermediate avg. Mass fraction
- **Ttot** – intermediate Avg. temp bath
- **Rey_sTot** – intermediate Avg. Rey_s
- **Y_reyTot** – intermediate Avg. mass fraction
- **Yavg** – Mass fraction avg.
- **Uavg** – bath vel. avg.
- **Tavg** – bath temp. avg.
- **alphaavg** – Avg. bath vol. fraction.
- **T_reyTot** – intermediate Avg. T_rey
- **T_rey** – velocity temp. fluc. correlation

OpenFOAM Input files For LES Study

FOLDER to specify thermal properties, fluid properties, interphase models,